This is to certify that the
dissertation entitled

CHARGE ACCUMULATION IMAGING OF A TWO-DIMENSIONAL ELECTRON SYSTEM

presented by

SUBHASISH CHAKRABORTY

has been accepted towards fulfillment
of the requirements for the

Ph.D degree in PHYSICS

Stuart Tessmer
Major Professor's Signature

7/29/03
Date

CHARGE ACCUMULATION IMAGING OF A TWO-DIMENSIONAL ELECTRON SYSTEM

By

Subhasish Chakraborty

A DISSERTATION

Submitted to
Michigan State University
In partial fulfillment of the requirements
For the degree of

DOCTOR OF PHILOSOPHY

Department of Physics and Astronomy

2003

ABSTRACT

CHARGE ACCUMULATION IMAGING OF TWO-DIMENSIONAL ELECTRON SYSTEM

By

Subhasish Chakraborty

In this thesis, we studied GaAs/AlGaAs two-dimensional electron systems (2DES) and quantum dots with a novel scanned probe method called charge accumulation imaging (CAI), in a tunneling geometry. We imaged the 2DES near integer Landau level filling and observed surprising density modulations, which gave rise to orientationally ordered stripe-like structures. These stripe-like structures were not static, but appeared as a function of the applied perpendicular magnetic field. We also imaged the 2DES in the absence of a magnetic field, to essentially image the disorder potential of the 2DES. Although theories predict a spatial distribution of the ionized donors to be truly random, micron size features were observed, consistent with similar experiments done in the presence of a magnetic field. Progress was made towards electron wavefunction imaging of quantum dots. Single-electron addition spectra of a disorder-induced quantum dot were observed with the CAI technique.

This thesis is dedicated to my parents.

ACKNOWLEDGEMENTS

This work would not have been possible without the generous support and assistance I received from my professors, colleagues, friends and family members. I consider myself extremely fortunate to have the opportunity to work under the supervision of my thesis advisor, Professor Stuart Tessmer. All through these years, he has been an outstanding teacher, showing extraordinary patience and support. Not only has he helped me countless time professionally; there have been several occasions when he helped me personally. For that I am indebted to him and consider him my very good friend.

Special thanks should go to Dr. Ilaari Maasilta, who taught me the technical details of the experiment, and from whose insight I have gained immensely. Thanks should also go to my lab-mates through the years – Sergei, Irma, Aleksandra and Cemil, for their day-to-day assistance and fun-filled discussion sessions. I should thank Ms. Debbie Simmons for her assistance on different occasions.

I should also thank Professor Norman Birge for his advice on the quantum dot fabrication. I am grateful to Dr. Khalid Eid and Dr. Baokang Bi for helping me with the fabrication process and scanning electron microscope. I am also grateful to Dr. Reza Loloee for his help on numerous occasions. I am thankful to the people of the machine shop, particularly James Muns, Thomas Hudson, and Thomas Palazzolo for their help and assistance.

Last but not the least, I am thankful to my family for their support and encouragement in pursuing a career in physics. My special gratitude goes to my wife,

Arunima. She has not only made countless sacrifices for my career, but has inspired and motivated me through the years.

This work was supported by the National Science Foundation grant Nos. DMR99-70756 and DMR00-7523 and the Alfred P. Sloan Foundation. The W. M. Keck Microfabrication Facility provided valuable resources for fabrication and scanning electron microscopy.

TABLE OF CONTENTS

LIST OF TABLES

LIST OF FIGURES

Chapter 1

Introduction

The two-dimensional electron system (2DES) trapped at a doped heterojunction is one of the most important systems for electronic transport. Not only is it at the heart of the technologically important field-effect transistors (FETs), but it is also a fascinating quantum system for the exploration of fundamental electron interactions. Thus, it has been an area of intense research for decades.

Most of the experiments on these systems have been what are called transport measurements, i.e., a current is passed on one direction of the sample, and the voltage both parallel and perpendicular to the current is measured. In the presence of a magnetic field perpendicular to the 2DES, these experiments have helped discover amazing physics, like the integer quantum hall effect (IQHE) [Prange, von Klitzing, Laughlin 1981] and the fractional quantum hall effect (FQHE) [Tsui, Laughlin 1983], the latter being one of the best known many-body phenomena. Si/SiO_2 and GaAs/AlGaAs are the most common two-dimensional electron system materials that have been studied over the years. While Si/SiO_2 FETs are the most common electronic devices, they have been largely superseded in the laboratory by GaAs/AlGaAs systems due to their very high mobility.

With the discovery of scanning tunneling microscopy (STM) [Binnig 1982, Binnig 1999] in the mid-eighties, and the advancement of other scanning techniques in the recent years, there has been a new direction in the study of the 2DES. The interest in imaging the 2DES with scanning techniques stems from some very exciting theoretical

work [Koulakov, Moessner]. Electronic transport measurements seem to verify some of these theories, but do not conclusively settle the issues. In some of the cases transport measurements are simply inadequate.

In this thesis, we shall focus on studying the 2DES with a scanning technique called the charge accumulation imaging (CAI) [Tessmer 1998, Levi, Finkelstein]. This Chapter continues with the introduction to physics of 2DES in perpendicular magnetic field, an introduction to charge density waves (CDWs) [Koulakov, Moessner] predicted by theories, and concludes with an introduction to the physics of zero-dimensional systems, popularly called quantum dots. The detailed theory along with experimental results for the CDWs and the quantum dots will be presented in Chapters 5 and 6 respectively. Chapter 2 discusses the samples and how they are grown; it also has some discussions of the physics of heterostructures that are known to most experts in the field. Chapter 3 covers the details of the technique of CAI and a subsection is devoted to the description of the experimental apparatus. The physics of disorder in 2DESs along with some interesting results will be described in Chapter 4, and Chapter 7 will summarize the experimental effort and future directions.

1.1 2DES in perpendicular magnetic field

The classical picture of the electronic motion in a transverse magnetic field is that the electrons move in circles, with the radius called the cyclotron radius R_C getting tighter with increasing magnetic field. This means the angular frequency of revolution, called the cyclotron frequency ω_C, increases with the field. Quantum mechanically, all the orbits are not allowed, leading to the formation of discrete states. The quantum mechanical problem

was solved long ago by Landau for two-dimensional spinless electrons in a magnetic field B [Prange]. Schrödinger's equation for such a system in the Landau gauge is given by:

$$\frac{\hbar^2}{2m}\left[\left\{\frac{1}{i}\frac{\partial}{\partial x}-\frac{eB}{\hbar}y\right\}^2-\frac{\partial^2}{\partial y^2}\right]\psi=E\psi. \tag{1.1}$$

The solutions with n = 0, 1, 2, 3, ... define the energy levels,

$$E_{nk}=\hbar\omega_C\left(n+\frac{1}{2}\right). \tag{1.2}$$

These energy levels are called the Landau levels (LL's). The spatial extent of the wave function is of the order of the magnetic length $\ell = (\hbar/eB)^{1/2}$. These Landau levels are highly degenerate and contain up to eB/h electrons and are separated by an energy of $\hbar\omega_C$. Now if we introduce impurities in the sample, many of the electrons in the 2DES might be under the influence of an impurity potential and thus may suffer a shift in energy. In addition if we have electric field, it causes some of the electrons to drift through the array of impurities. Solving the problem of 2DES in an in-plane electric and perpendicular magnetic field under the influence of impurity potentials, we find that the degeneracy of LL's is completely lifted. The density of states evolves from sharp LL's to a broader spectrum of levels as the impurity potential is turned on (see Figure 1). The various quantum states in each energy band can be divided into two general classes. The states near the top and bottom of each band, are localized in small regions of the sample. These localized states occur in regions around impurity atoms that have an excess of positive or negative charge. Near the center of each band are the so-called extended

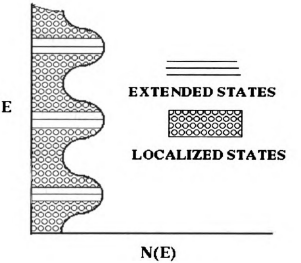

Figure 1. The extended and localized states in the Landau bands.

states, each being spread out over a large region of space. The density variations shown in Figure 1 also lead to compressibility variations. Compressibility is a measure of the energy required to add an electron to the 2DES. Mathematically, we define compressibility as $d\rho/d\mu$, where ρ is the electron density per unit area and μ is the chemical potential. At integer filling, the system is less compressible. Here, the Fermi level is in the region of lower density of states (the dip in the trace in Figure 1), so adding an electron in this region will shift the Fermi level more than if we are at regions further from integer filling. This fact has important consequences for our measurement.

1.2 Charge Density Waves

Before we proceed further, let us define a quantity called the filling factor $\nu = \rho h/eB$, where h is the Planck constant and e is the electron charge. The quantum Hall effect is different from its classical analog. If we plot the Hall conductance versus the reciprocal of the magnetic field, it shows distinct plateaus at certain values of ν, instead of a straight line. For integer values of ν, the phenomenon is called the integer quantum Hall effect (IQHE) [Prange, von Klitzing, Laughlin 1981], whereas plateaus at fractional values indicate fractional quantum Hall effect (FQHE) [Tsui, Laughlin 1983]. The FQHE was first discovered at the lowest Landau level ($\nu < 1$), and typically occurs at odd denominator values of filling factor, $\nu = 1/3, 1/5$, etc. This effect has been identified with the formation of a uniform incompressible quantum state, called the Laughlin liquid. At weaker magnetic fields, or at higher filling factors ($\nu > 4$), the Laughlin liquid fails to be the ground state of the system. Hartree-Fock calculations show that in the case of higher filling factors a phase called the "bubble" phase wins over the Laughlin liquid [Koulakov,

Fogler 1997, Fogler 1996]. Intuitively, there is a competition between the long-range Coulomb repulsion and the short-range exchange attraction among the electrons in the uppermost partially-filled Landau levels. The best compromise for the electrons is to form clusters or "bubbles", and calculations show that they would form a triangular lattice. As we keep on adding electrons to the system, the bubbles grow in size, finally to coalesce to form what is called the "stripe" phase [Koulakov, Fogler 1997, Fogler 1996]. On the other end, for the few electrons in the uppermost level, the "bubbles" contain only one electron; this is a type of Wigner crystal. The three together are called the charge density wave phase, shown in Figure 2. The goal of the experiment is to resolve these charge density wave patterns with the CAI scanning probe technique.

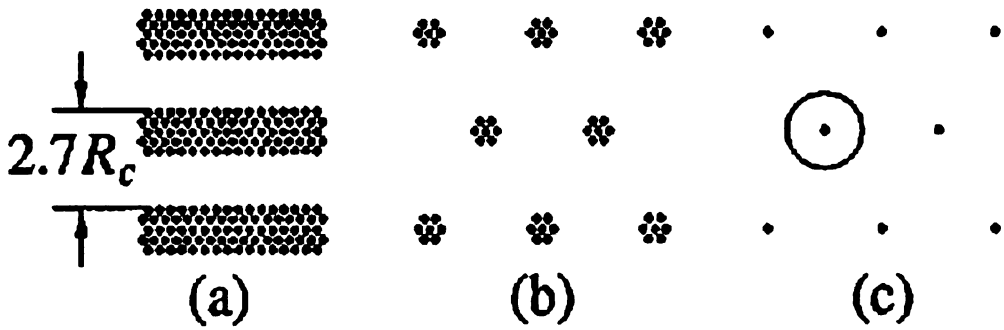

Figure 2. Theoretically predicted CDW patterns [Koulakov]. (a) Stripe pattern. (b) Bubble pattern. (c) Wigner Crystal, showing one cyclotron orbit. The spacing of $2.7R_C$ between the stripes is at $\nu \approx 4$.

1.3 Quantum Dots

Quantum dots are small structures in a solid, with sizes of the order of few tens of nanometers to a few microns [Kastner, McEuen, Kouwenhoven 2001]. They consist of 10^3-10^9 atoms and an approximately equal number of electrons. In a semiconductor, most of these electrons are tightly bound to the nuclei except for a very small number. Current nanofabrication technology allows us to precisely control the size and shape of these dots. Metallic gates are patterned on the semiconductor with electron beam lithography to define a quantum dot. Another common technique in use is etching, in which semiconductor material is selectively removed to form a quantum dot. The confining potential in a quantum dot is usually bowl-like or parabolic, in which electrons tend to fall in towards the bottom of the bowl. The confinement of electrons is therefore, in all three spatial directions, resulting in a quantized energy spectrum – much like an atom. Hence they are also called artificial atoms. One can consider the quantum dot as a tiny laboratory in which quantum mechanics and the effects of electron-electron interactions can be studied.

Quantum dots have been an area of fruitful research for a long time. A lot of research has gone into probing the energy levels of the individual quantum dots, mostly by gated transport or capacitance spectroscopy [Reed, Meirav, Main, Gueret, Schmidt, Tarucha]. For example, a classic experiment done by Ashoori *et al.* [Ashoori 1996] is shown in Figure 3. This experiment probed the transitions between energy levels of a quantum dot by precisely controlling the number of electrons contained in the dots, down to as few as one electron. While these measurements have yielded a wealth of information about electronic transitions and the effect of electron-electron interactions,

many questions remain unanswered. Studying the spatial structure of the electron probability density represents a new way to probe the eigenstates. However, such a study would require new techniques. We use Charge Accumulation Imaging in a configuration that allows for the possibility of mapping out the spatial charge distribution of individual electrons, and also studying the addition spectrum of electrons in quantum dots.

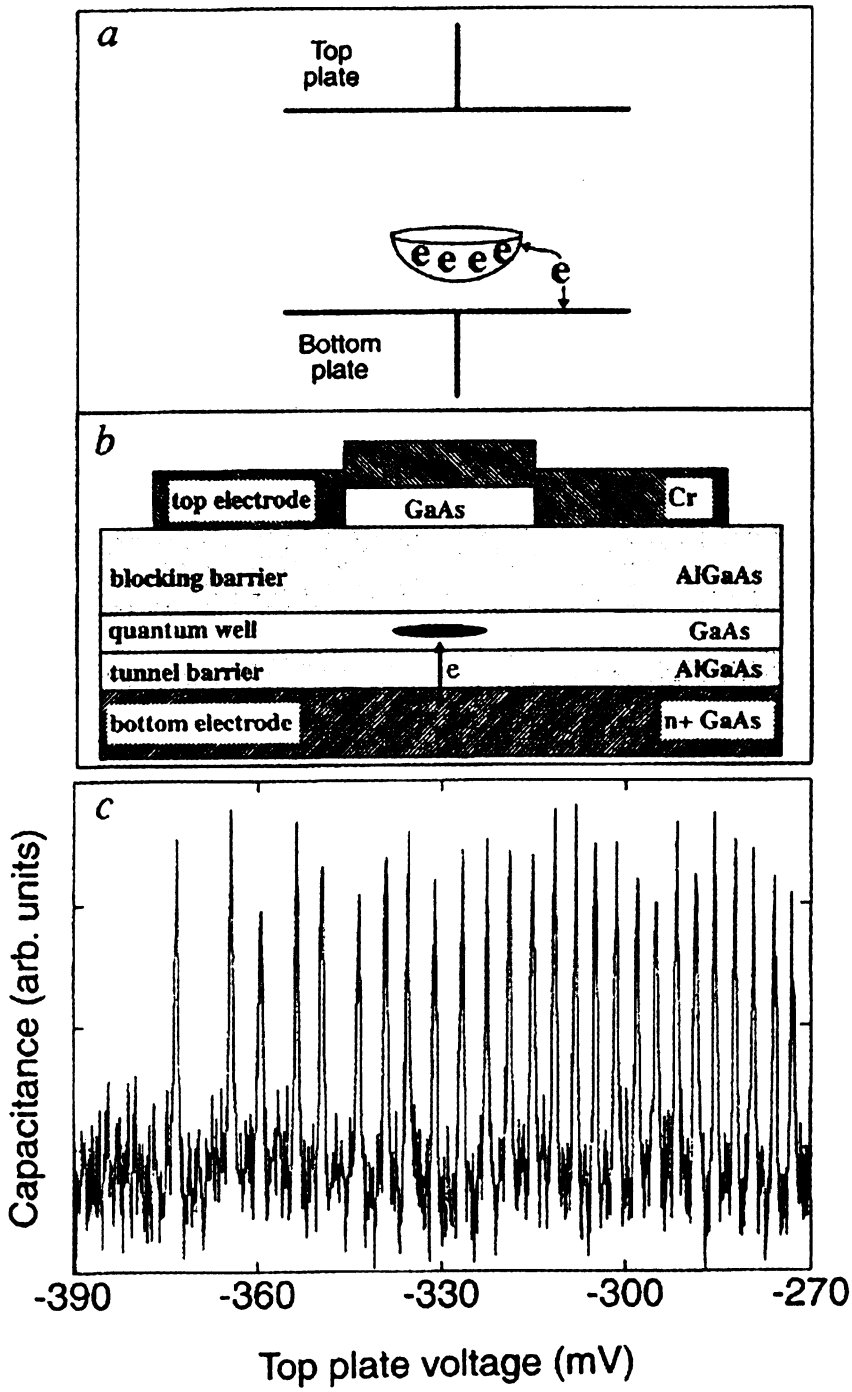

Figure 3. (a) Schematic diagram of an artificial atom located between two capacitor plates. (b) Diagram of the sample used by Ashoori et al., the black disk is the artificial atom in the quantum well. (c) Capacitance of the sample as a function of the top plate voltage, each spike in the plot represents individual electrons entering the dot at a particular gate voltage, which corresponds to the energy required to add an electron to the system. Thus the plot is the addition spectra of the artificial atom [Ashoori 1996].

Chapter 2

Heterostructures

Heterostructures are semiconductors composed of more than one material [Davies]. The high mobility 2DES is realized at the interface of two materials forming the heterostructure. One of the materials has a wider bandgap than the other, and a slight doping of one layer produces an electric field, essential to bend the bands forming a quantum well at the interface and the electrons given up by the dopant atoms form the 2DES. The most common heterostructures are made out of III-V semiconductors. The conditions to be good candidates for the two materials to form a heterostructures are that they have the same crystal structure or at least the same symmetry, and that they have nearly identical lattice constant to minimize strain in the final structure. Gallium arsenide (GaAs) and aluminium gallium arsenide (AlGaAs) meet these criteria, and form one of the mostly commonly used III-V heterostructures.

The 2DES are typically formed at or close to the interfaces of the heterostructure, as mentioned above. This puts a stringent condition on growth that the interface be nearly perfect. Any imperfection would result in scattering of electrons as they travel along the interface, decreasing the mobility. Thus heterostructures should have an atomically sharp interface if they are to perform well. Additionally, the layers are usually very thin and require changing of composition very rapidly during growth. Also the interface must be contamination free. Hence, it is a challenge to grow such structures. The most common growing technique is the molecular-beam epitaxy [Davies]; with which it is possible

grow highly abrupt junctions between different materials. It also allows atomic scale control over the thickness of layers.

2.1 Molecular-beam epitaxy

Samples used in this study were grown by molecular-beam epitaxy by Prof. M. R. Melloch at Purdue University. Molecular-beam epitaxy or MBE is very simple in principle. The substrate is heated on a holder, which sits inside an ultra-high vacuum (UHV) chamber. The elements that compose the heterostructure are vaporized in individual furnaces with orifices directed towards the substrate, but shielded from it by shutters. These furnaces are called the Knudsen cells or K-cells. The reasons for the substrate to be in UHV are twofold. Firstly, contamination has to be avoided during growth. And more importantly, UHV ensures that the molecular flow regime holds. In the molecular flow regime, the mean free path of a molecule is much longer than the length of the chamber, so that it never suffers a collision in its path from the K-cells to the substrate. Hence the molecules that emerge from the K-cells do not diffuse as in a gas at higher pressure, but form a molecular beam traveling straight without collisions to impinge on the substrate. Growth starts once the shutters of the K-cells are opened and the temperature of the cells controls the flux of each element. To ensure uniform growth across the substrate, the sample holder is rotated during growth. Dopants are added using additional cells.

MBE is a very slow process, and grows material about 1μm per hour. The growth is monitored using a technique called reflected high-energy electron diffraction or RHEED. With RHEED, growth can be counted precisely in monolayers, and it also reveals the structure of the surface. A very simplified schematic of a MBE machine is

shown in Figure 4. MBE machines produce very high quality GaAs/AlGaAs samples. The quality of a semiconductor sample is determined by its electron mobility. The next section describes what is meant by mobility.

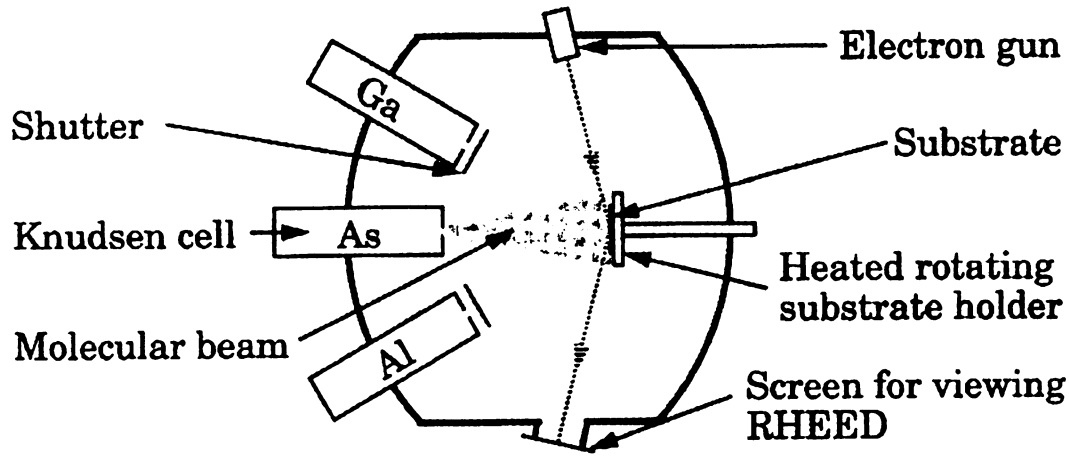

Figure 4. Schematic diagram of an MBE machine showing Knudsen cells for Al, As and Ga with shutters. The sample sits on a heated holder, which is rotated. The RHEED apparatus is also shown [Davies].

2.2 Mobility

Mobility is a very important quantity in characterizing semiconductor materials. It describes the ease with which electrons drift in materials in response to an electric field. Following the Drude model [Ashcroft], the electrons in a solid are in constant random motion. Since the motion is random, there is no net displacement of the electron over a period of time. Of course, this is only true for a large number of electrons, and not any individual one. Hence in the absence of an electric field, there is no net current. Now if an electric field E_X is applied in the x-direction, then each electron experiences a force $-eE_X$, and there is a net motion in the x-direction. If p_X is the x-component of the total momentum, then for n electrons/cm^3, the force of the field is

$$-neE_X = \frac{dp_X}{dt}. \tag{2.1}$$

However, the net acceleration of equation (2.1) is just balanced by the decelerations due to collision, for steady state current flow. The probability that any electron has a collision in the time interval dt is given by dt/τ, where τ is the relaxation time. Thus the differential change in momentum p_X in time dt, due to collisions is given by:

$$dp_X = -p_X \frac{dt}{\tau}. \tag{2.2}$$

Hence rate of change of momentum of electrons due to collisions is

$$\frac{dp_X}{dt} = -\frac{p_X}{\tau}. \tag{2.3}$$

For steady state current, equations (2.1) and (2.3) should add to zero, so that the average momentum per electron is

$$< p_X > = \frac{p_X}{n} = -e\tau E_X . \qquad (2.4)$$

The mobility μ is defined as the average drift velocity per unit electric field or

$$\mu = -\frac{< v_X >}{E_X} = -\frac{< p_X >}{m^* E_X} = \frac{e\tau}{m^*}. \qquad (2.5)$$

Where m^* is the effective mass and v_X the average drift velocity of the electron. The minus sign in the definition of μ in equation (2.5) ensures that μ is positive, since electrons drift opposite to the field. The unit of mobility derived from its definition is cm^2/ V-sec.

2.3 Formation of 2DES and modulation doping

As mentioned earlier 2DES is formed at the interface between two semiconductors. In this section, we shall discuss the formation of the 2DES in the GaAs/ AlGaAs heterostructure [Davies, Prange]. The principle is quite simple. An atomically perfect interface of GaAs and AlGaAs is grown with MBE. Because the conduction band has an abrupt step at the interface, an electric field perpendicular to the interface attracts electrons into a quantum well created by the field and the interface. The motion perpendicular to the interface is quantized and is therefore frozen out, if all electrons are in the lowest state. This results in a two- dimensional electron system. The electric field perpendicular to the interface is achieved through doping. With MBE atomically perfect layers of GaAs are grown, followed by a sequence of AlGaAs. The two materials have nearly the same lattice and dielectric constants. Without taking into consideration the effect of the dopants, the band would be as shown in Figure 5.

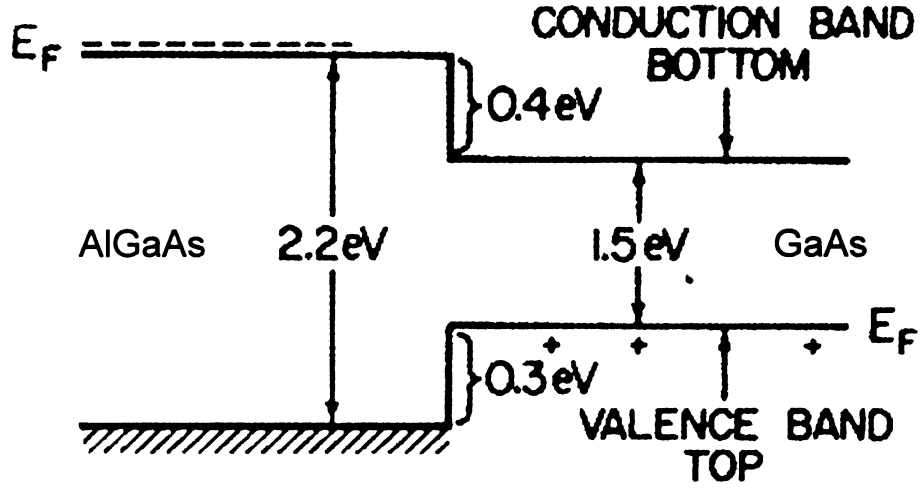

Figure 5. The energy-level diagram of AlGaAs and GaAs without taking into consideration certain electronic processes [Prange].

The AlGaAs is deliberately doped n-type, so that it has mobile electrons in its conduction band. GaAs is typically p-type, with few holes in its valence band. The electrons in the conduction band of AlGaAs migrate to fill in these holes, but usually end up at the bottom of the conduction band of GaAs. However, positive charge is left on the donor impurities due to migration, which attracts these electrons back toward the interface and bends the band in the process, forming a quantum well. This is the source of the electric field in this system. The transfer of electrons from AlGaAs to GaAs will continue until the dipole layer formed from the positive donors and the negative inversion layer is sufficiently strong. The dipole layer thus formed makes the Fermi level of the GaAs equal to that of AlGaAs. The density of electrons in the quantum well is determined by the dopant density. Figure 6 shows the energy-level diagram for the formation of the quantum well described above.

An important part of this technique is to implant the donors in the AlGaAs physically as far away from the interface as possible. This reduces the scattering of electrons in the well by the positive donors and increases the mobility of the 2DES many fold. This kind of doping is called remote or modulation doping. A refinement made by leaving a spacer layer of undoped AlGaAs between the n-AlGaAs and GaAs, increases the separation between the electrons and the donors. This further reduces the scattering and increases the mobility of the 2DES, but at the cost of a lower density of electrons. High mobility is of utmost importance while studying the physics of 2DES.

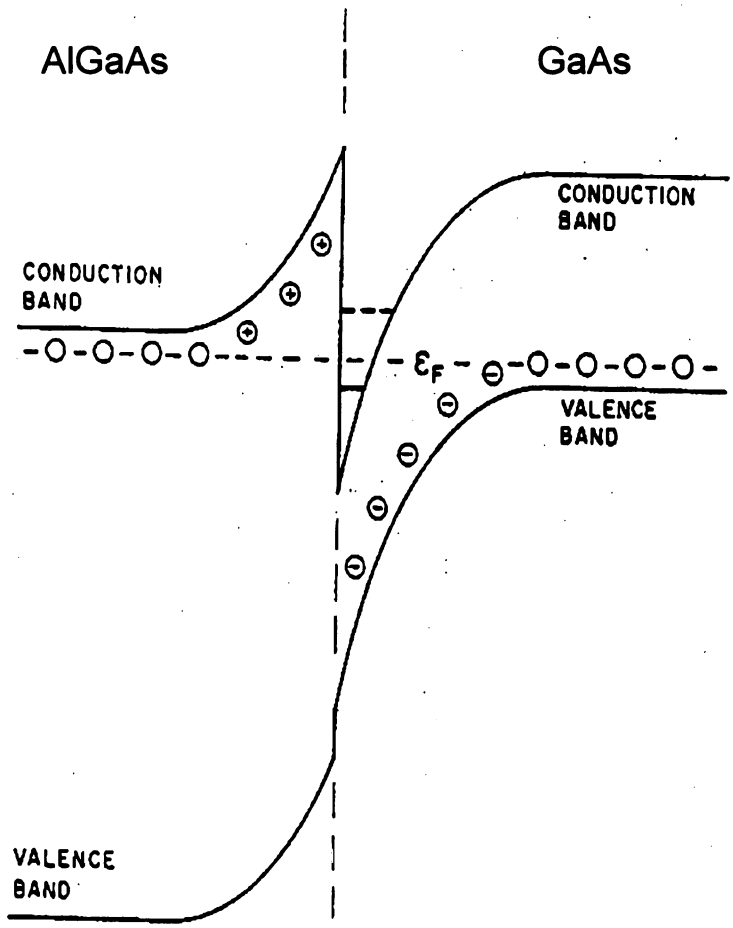

Figure 6. Energy-level diagram of a GaAs/AlGaAs heterostructure. The donor electrons tunnel through the potential barrier and occupy the first conduction sub-band of the potential well. The Fermi level is shown as ε_F. The spacer layer is not shown [Prange].

2.4 The Sample

The sample and the tip used in the experiment, is shown in Figure 7. The sample is a GaAs/AlGaAs heterostructure grown with MBE technique as described in section 2.1. The 2DES is formed at the interface of GaAs and AlGaAs. There is no ohmic contact to the 2DES, instead there is a metallic substrate below the 2DES and separated from it by a tunnel barrier. The metallic substrate is a heavily doped n-type GaAs, and the tunnel barrier is composed of layers of undoped AlGaAs. A sinusoidal voltage is applied to the metallic substrate, in response to which electrons tunnel into the 2DES just below the apex of the tip. This tunneling produces an image charge on the tip, which is measured. The details of the technique are discussed in the next Chapter. The 2DES sits approximately 60 nm below the surface of the sample and 40 nm above the metallic substrate. The mobilty of the sample was 10^5 cm^2/V-sec, and the average density was 6 x 10^{11} cm^{-2}.

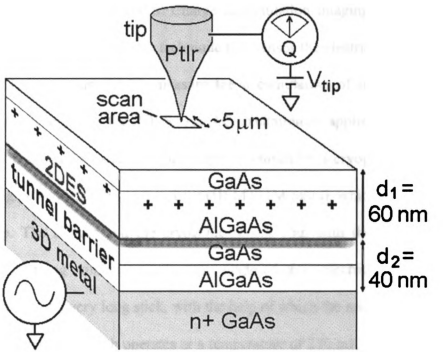

Figure 7. The sample and the tip. The typical scan area is 5μm x 5μm.

Chapter 3

Experimental technique and apparatus

Two-dimensional electron systems are formed in GaAs, tens of nanometers below the surface of a heterostructure sample. Hence, scanning tunneling microscopy (STM) [Binnig 1982, Binnig 1999] and other techniques that probe the surface are not adequate to probe the interior of a 2DES. Charge accumulation imaging (CAI) [Tessmer 1998, Levi, Finkelstein] is a cryogenic technique that senses the electric field emanating from a sample. Hence, it can locally measure the accumulation of mobile charges within a conducting system like the 2DES. An AC excitation is applied to the sample, and a metallic tip is scanned over it. The charge is sensed by a cryogenic sensor constructed from a high electron mobility transistor (HEMT) [Mimura], which is mounted very close to the tip. The sample and the cryogenic sensor chip with the tip are mounted on a modified scanning tunneling microscope, made of piezo-electric tubes. The microscope sits at the end of a very long stick, with the help of which the microscope is dipped into a liquid He3 cryostat, which operates at a temperature of 270 mK. The rest of this Chapter describes in detail the CAI technique, the scan head, the charge sensor and the cryostat.

3.1 Charge Accumulation Imaging

Charge accumulation imaging is essentially a capacitive measurement. As shown in Figure 8, the tip and the sample can be thought of as the two plates of a parallel plate capacitor. As a voltage is applied to the sample, an image charge is induced on the tip. The charge sensor attached to the tip measures this image charge. This technique was

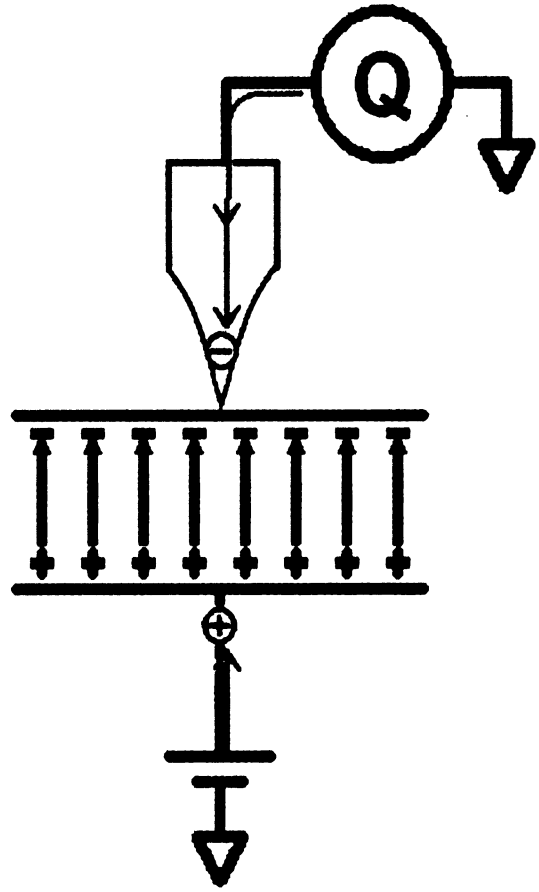

Figure 8. Schematic of the CAI technique. CAI is a capacitive technique in which the tip and the 2DES can be thought of as the two plates of a capacitor, with a voltage being applied to the 2DES that charges up the tip.

first developed by S. H. Tessmer *et al* [Tessmer 1998]. They imaged random droplet patterns that mirrored the static disorder potential of the 2DES in GaAs/AlGaAs heterostructure. The important difference from the earlier experiment is that, they had a direct Ohmic contact to the 2DES, as mentioned in Chapter 2. Instead, in the measurements described here, our sample has a metallic substrate approximately 40nm below the 2DES. This 3D-to-2D tunneling arrangement is shown in Figure 9. An AC excitation of 8mV at a frequency of 20KHz is applied to the metallic substrate. In response to the AC excitation, electrons tunnel from the metallic substrate to the 2DES. This induces an image charge on the tip, which is measured by the sensor circuit (described in section 3.3). The advantage of this technique over its predecessor [Tessmer 1998, Levi, Finkelstein] mentioned above is significant. If the 2DES is mostly non-conducting, which happens if the magnetic field is such that the 2DES is close to integer Landau level filling, a direct contact to the 2DES would prevent the electrons from reaching the region below the apex of the tip, and the signal would vanish. Thus the technique is not useful in imaging of 2DES structures when its bulk is nonconducting. The technique employed in our measurement, on the other hand, is local in the sense that even if the 2DES is non-conducting as a whole electrons are able to enter the conducting pockets in the 2DES by tunneling from the metallic substrate. Hence we are able to resolve structures in the 2DES at magnetic fields, when the system is close to integer filling, and is mostly non-conducting. Another important feature of this technique is that we are sensitive to electron correlation effect, which can only be measured in tunneling experiments. Ashoori *et al.* [Ashoori 1990] and Eisenstein *et al.* [Eisenstein] have found that electron correlations give rise to a Coulomb psuedogap in the tunneling density of

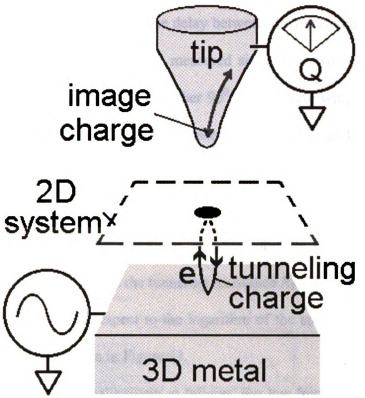

Figure 9. Schematic of the 3D-to-2D CAI technique. Here an AC excitation is applied to the 3D metallic substrate separated from the 2DES by a tunneling barrier, instead of a direct Ohmic contact to the 2DES. The charge tunneling into the 2DES induces an image charge on the tip, which is measured.

states of the 2DES. A more detailed description and experimental results pertaining to the psuedogap physics will be discussed in Chapter 5.

As we apply the AC excitation to the metallic substrate, the tunneling into the 2DES is not instantaneous; there is a time delay between the measured charge on the tip and the applied AC excitation. Thus the measured signal has two components, one in phase with the applied excitation and the other 90^0 out of phase with it. We call the in-phase capacitance signal Q_{in}, and the out-of-phase signal Q_{out}. Figure 10 shows the actual tip-sample arrangement and the equivalent circuit. For simplicity, the capacitance between the tip and 2DES can be thought of as a parallel plate capacitor C_{tip}. Similarly the capacitance between the 2DES and the metallic substrate is another parallel plate capacitor C_T, which is in parallel to the tunneling resistance R_T. These form an RC circuit. The plot of Q_{in} and Q_{out} with respect to the logarithm of the applied frequency f or the tunneling resistance R_T is shown in Figure 11.

The plots can be understood qualitatively as follows. For low frequencies, the charge has enough time (compared to the time constant of the RC circuit) to tunnel into the 2DES and thus stays in phase with the applied AC excitation. Hence the in-phase signal, which is purely capacitive, dominates, while the out-of-phase signal is almost zero. As the frequency is increased, the excitation period becomes comparable to the RC time constant, and the measured signal goes out of phase with the applied excitation. Hence the signal shows up mostly in the Q_{out}, which peaks at a certain value of the frequency f_0, while the Q_{in} rolls off. As the frequency is further increased, the excitation period is very short compared to RC and the charge has almost no time to tunnel into the 2DES. Hence both the in-phase and the out-of-phase signal go down.

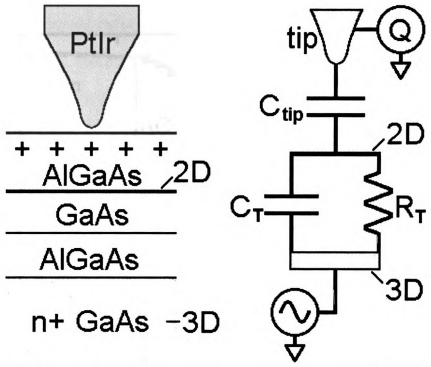

Figure 10. The circuit equivalent to the tip sample arrangement in the 3D-to-2D CAI technique.

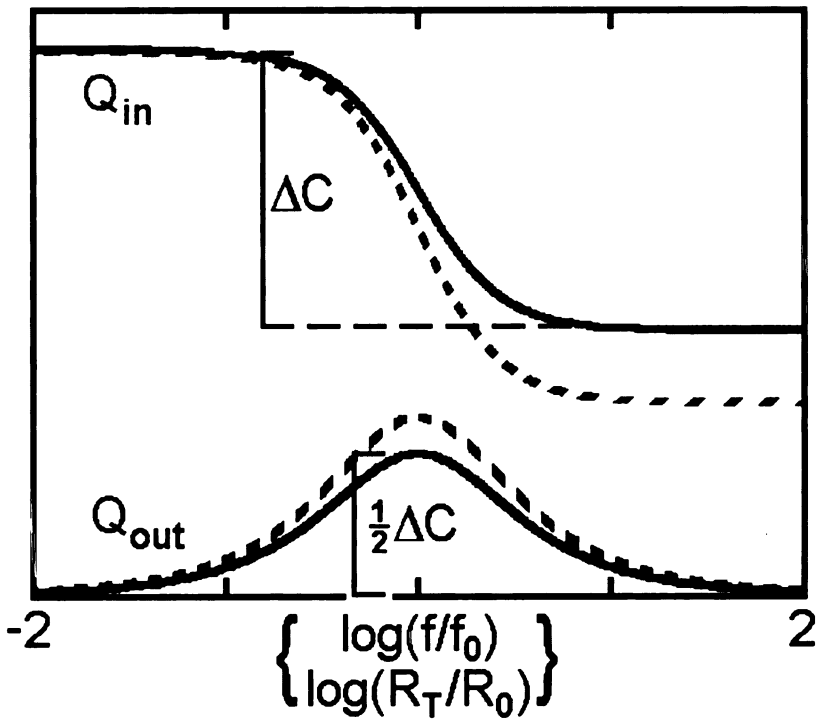

Figure 11. The in-phase and the out-of-phase charging as a function of logarithmic frequency and tunneling resistance, as obtained from the model circuit. The dashed curves are the charging when in-plane conductivity is taken into consideration.

A Similar argument holds for the in-phase and out-of-phase signal versus the tunneling resistance. Thus the charging components have identical functional dependence on the frequency f and the tunneling resistance R_T, with characteristic values of $f_0 = \frac{1}{2\pi R_T (C_T + C_{tip})}$ and $R_0 = \frac{1}{2\pi f (C_T + C_{tip})}$ respectively. The magnitude of the curves is set by the tip-sample capacitance difference ΔC between a fully charging and locally non-charging 2DES. More rigorous modeling [Maasilta, personal communications] for the system considers the distributed nature of the tip-sample capacitance and the effect of charge motion within the 2D plane. Such models show an enhancement in the charging characteristics as the in-plane relaxation rates approach the tunneling rate, an effect that may occur near integer filling, as indicated qualitatively by the dashed curves. Figure 12 shows a plot of the differential change of the in-phase and the out-of-phase components with respect to the tunneling resistance versus frequency of the applied excitation. As can be seen, the out-of-phase signal is more sensitive to the change in tunneling resistance than the in-phase, at low frequencies. In Chapter 5, we shall apply this model of the tip and sample circuit to explain some of our experimental observations.

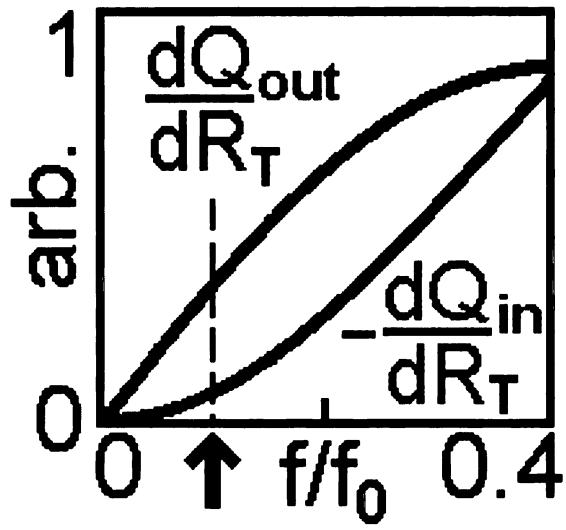

Figure 12. The differential change in the in-phase and the out-of-phase charging with respect to the change in the tunneling resistance plotted against the frequency. At the low frequency limit, the out-of-phase component is more sensitive to changes in tunneling resistance.

3.2 The scan head

The goal of a scanning tunneling microscope (STM) [Binnig 1982, Binnig 1999] is usually to get atomic resolution surface topography or high quality spectroscopy. Achieving that goal would require very high stability of the scan head, which leads to small piezo lengths and hence small scan ranges. The physics that was studied in our experiment not only requires hours of stable operation, but also a micron-scale scan range. Hence conventional STM is not suitable for our experiment. It is actually a challenge to build a piezo-electric based microscope with high stability, without compromising on its scan range. Since we use a direct immersion He3 cryostat to cool down the sample, there is an additional issue. In conventional Besocke (see Figure 13) design [Besocke], the sample rests on top of piezo tubes. Therefore using long piezo tubes to achieve big scan ranges not only compromises the stability, but also keeps the sample at a high position relative to the bottom of the scan head. As a result, for direct immersion in liquid He3, the liquid level may soon drop down below the level of the sample, causing the sample to warm up before any meaningful data can be acquired. Alternatively, a scheme [Tessmer 1998] in which the sample sits relatively low on the scan head, with a long scanning piezo coming from the top as shown in Figure 14, seems to be a good idea. The drawback of this design is its thermal instability. Since the thermal contraction of a metal body is much greater than that of the piezo-electric tubes, temperature changes can cause the tip to crash into the sample. Even minute thermal instabilities at the base temperature can cause significant drift in tip-sample separation.

To fulfill all the three requirements, namely high thermal stability, high scan range and sample sitting as close to the bottom of a scan head as possible, we have

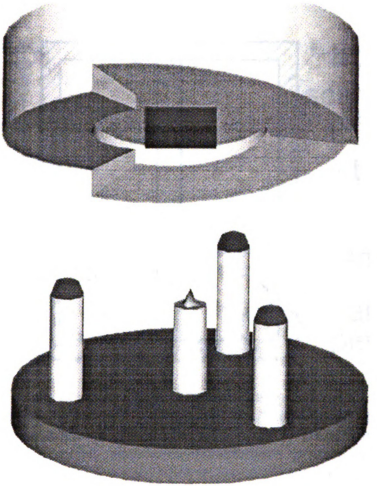

Figure 13. Schematic of the Besocke design. The sample sits on top of the three carrier piezo tubes, which along with the scanning tube is attached to a bottom plate. The ramps face the same side as the sample.

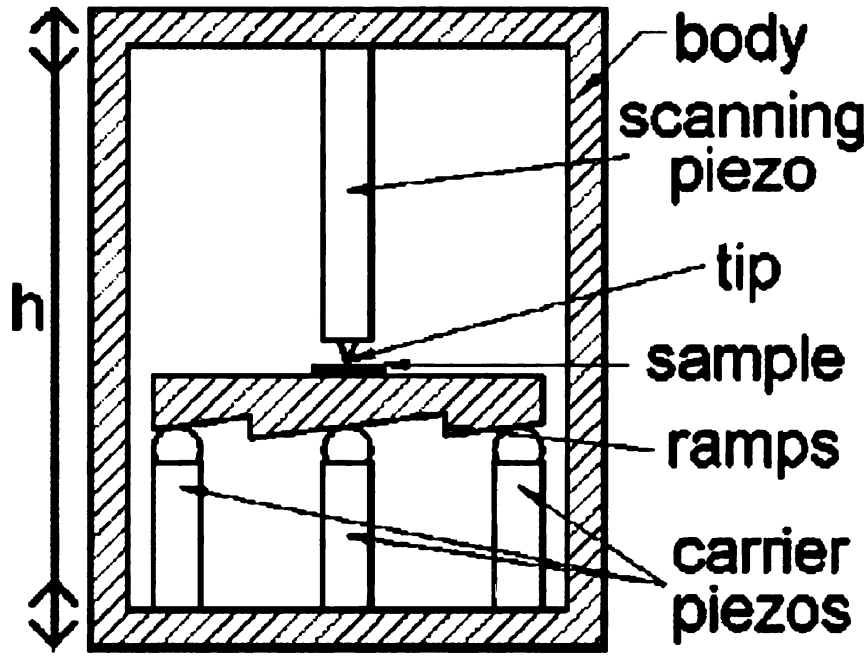

Figure 14. Schematic of a microscope design utilized by few experiments. The thermal-contraction mismatch between the metal body (hatched) and piezoelectric tubes represents a major drawback. Essentially, in response to temperature fluctuations, the body expands and contracts much more than the piezo ceramic. These uncompensated fluctuations in height h result in significant variations of the tip-sample separation.

designed and built a novel scan head [Urazhdin 2000]. A schematic of the design is shown in Figure 15, and the actual microscope is shown in Figure 16. The novelty of the design is that both the three piezo tubes holding the sample and the one scan tube are soldered to a top plate. This essentially solves two of the three problems – thermal instability and He3 level dropping below the sample too soon. The sample and the tip are attached to identical piezo tubes. Thermal contraction of the three carrier piezo tubes, which tend to move the sample towards the tip, is compensated by the tip moving upwards, away from the sample as the scanning tube to which the tip is attached contracts by the same amount. Thus temperature changes do not affect the tip-sample separation. Also, as seen from the schematic, the sample sits almost at the bottom of the microscope; hence the microscope only warms up when the sample space in the cryostat runs out of liquid He3. Lastly high scan range can be achieved by having all the piezo tubes very long, without compromising on any of the above requirements. The piezo tubes are 7.6 cm long and are soldered to a brass base plate, which is rigidly attached to a very long stainless steel stick. The sample rests on the small feet that are part of the cylindrical legs, as indicated in Figure 15(a). A mechanism inside the legs allows for the rotation of each supporting foot by 180^0. This allows for the brass displacer, used for screening electric field of the piezo tubes, to be installed and removed. Each leg consists of a piston rigidly attached to the foot, and a small Be-Cu compression spring. The resulting upward pressure on the piston presses the supporting piece against the leg, without limiting its rotational motion. This is shown in Figure 15(b). A groove made in the leg fixes the piece in two positions, directed inward or outward. The sample holder diameter is slightly bigger than the opening between two legs. Hence two out of the three legs are notched

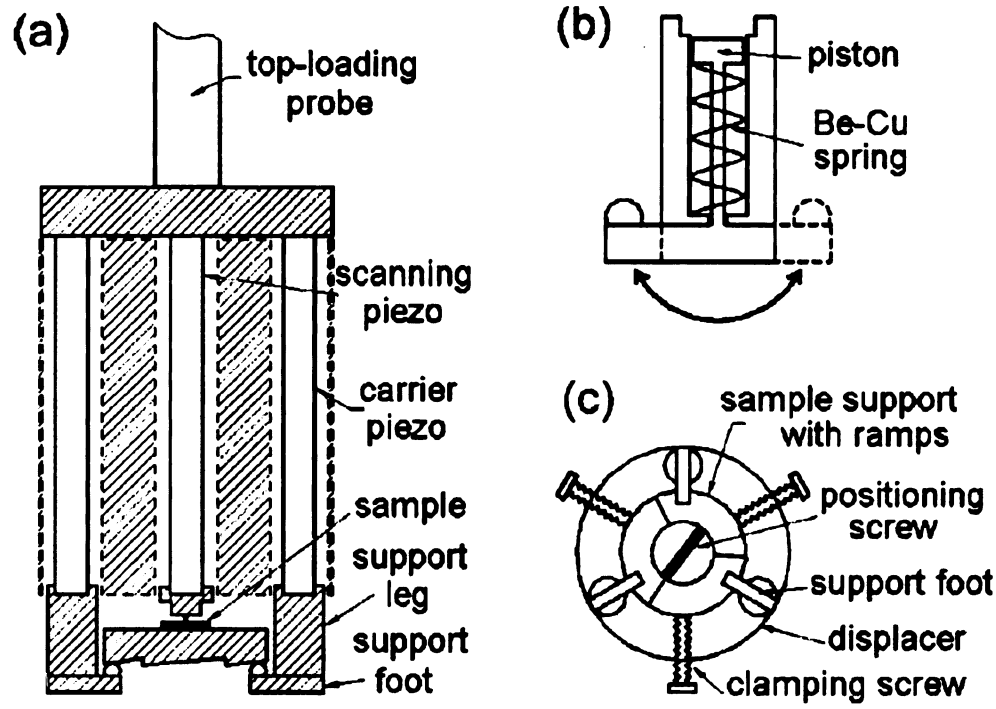

Figure 15. (a) Schematic of scanning head. Both the tip and the sample are supported by identical piezoelectric tubes (dimensions: 7.6cm-long x 4.8mm-diam x 0.8 mm wall thickness). As a result the unit is nearly perfectly thermally compensated. The displacer, outlined in dashes, screens the tip from the electric fields of the piezo tubes. All the metal parts are made of brass, shown hatched. (b) Sketch of support leg showing the rotating foot assembly. (c) Bottom view of the microscope. The clamping screws fix the ramps to allow the positioning screw to be turned—the sample is attached to the other side of this screw. In this way, we can adjust the vertical position of the sample by as much as 1 cm. The diameter of the unit is 3.8 cm.

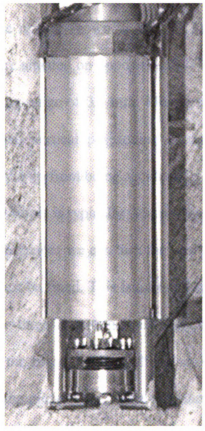

Figure 16. Photograph of the actual microscope. The shiny ruby balls at the end of each foot help reduce friction during fine approach of the sample.

longitudinally, and the sample is mounted through the gap between them.

Figure 15(c) shows a bottom view of the assembly. The sample holder is similar in design to the Besocke ramps (shown in Figure 13) [Besocke] except that the sloped ramps and the sample are situated on opposite sides. We chose a slope of 2°, yielding a coarse vertical positioning range of 0.4 mm. Moreover, the sample sits on a positioning screw that allows manual vertical positioning in the range of almost 1 cm. This is important in preventing the tip from being accidentally crashed during the insertion of the sample. In practice, the sample is typically 0.5 cm from the tip after initially inserting the sample holder. Of course, before we can turn the positioning screw to bring it closer, the position of the ramps must be fixed. This is accomplished by pinching the sample holder from the sides using the three clamping screws, shown in Figure 15(c). The clamping screws are attached to the brass displacer that also serves to screen the electric field generated by operating the piezo tubes. After the clamping screws are removed, an end cap is put in place. The interior of this cap provides a smooth surface for contact with the sides of the sample holder. We ensure low friction by applying MoS_2 powder to the interior surface of the cap in addition to the sides and the ramps of the sample holder. The microscope is cooled by slowly lowering the probe into the cryostat -- achieving a cooling rate of 1 K/min. There is little risk of mechanical vibrations causing a crash during this procedure, as gravity tends to pull the sample away from the tip. Finally, the fine sample approach is achieved by the standard inertial walking procedure utilized in Besocke-type designs. We find our scanning piezo tube (7.6-cm-long x 4.8-mm-diam x 0.8 mm wall thickness) to have a sensitivity of 1300 Å/V laterally and 73Å/V vertically at liquid-helium temperatures. Using commercially purchased electronics, which provide

a voltage range of ±130 V, we thus achieve an impressive cryogenic lateral scan range of 34 μm. The same large range of motion of the carrier piezo tubes also enables us to do the fine sample approach very quickly. Typically, the full range of the ramps is traversed in approximately 2 min at liquid-helium temperatures. We find the microscope to be sufficiently stable to function without a low-temperature vibration isolation stage. With regard to the entire cryostat, we have taken care to minimize building vibrations using a bungee cord suspension system. Mechanical pumps, which are part of the cryogenic system, represent a major source of additional vibrations. We have decoupled those modes by using tubing that has a section made of flexible rubber, connected to a section of stainless steel. That produces an impedance mismatch so that part of the vibrations is reflected at the junction [Movsovich]. We have also connected the tube rigidly to a heavy lead block at one point and immersed it into a sandbox at another.

Figure 17(a) shows a 35μm x 35μm topographic image of a platinum sample with a grid of 5μm x 5μm pits that are 1800Å deep, obtained in tunneling mode with the microscope at room temperature. This is how we calibrate the piezo tubes of our microscope. The 35μm scan range is approximately the maximum range at liquid-helium temperatures. Figure 17(b) shows line scans across a single pit measured in both tunneling and capacitance modes. For the capacitance scan no feedback was used; the tip was simply scanned above the sample in a straight line. The tunneling mode clearly has better resolution, comparing the sharpness of the walls. This is natural because tunneling takes place only at the apex of the tip on atomic scale, whereas the resolution in the

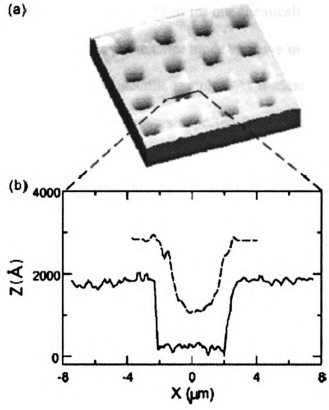

Figure17. (a) A 35 μm x 35 μm topographical image of a platinum sample with a grid of 5 μm x 5 μm pits that are 180 nm deep, obtained at room temperature. (b) Cross section across a single pit measured both in the tunneling mode (solid line) and in capacitance mode (dashed line).

capacitance mode is determined by distance between the tip and the sample and by the radius of curvature of the tip's apex, ~50nm for our chemically etched tips. Nevertheless, Figure 17(b) also shows that the capacitance mode can give us more information than just the topography, even for simple metallic samples. As is clearly visible, capacitance has local maxima at the edges of the pits, as expected from electrostatics (because electric field is higher around sharp corners).

3.3 The cryogenic charge sensor

Bipolar junction transistors (BJTs) are useless for low temperature applications because at temperatures below 100K there are almost no charge carriers in the conduction band to carry current. Field effect transistors (FETs) perform better than BJTs at low temperatures, but the power dissipated by such devices is typically in the mW range, which is too large a heat load for He3 based cryostats. High-electron mobility transistors (HEMTs) [Mimura] are GaAs/AlGaAs based modulation doped heterostructure devices, which are well suited for cryogenic operations. These are very similar to the commonly used FETs, except that the source-drain channel is a two-dimensional electron system, just like the system studied in the experiment. Since the 2DES is the channel for the HEMTs, they do not have to depend on thermally activated carriers like the BJTs, and hence do not suffer carrier freeze out at low temperatures. Moreover, since the only source of scattering for its charge carriers is the dopant atoms, as temperature is lowered, these dopants freeze out, increasing the mobility of the charge carriers. These devices can be operated in the Ohmic region, far away from saturation, reducing the power

dissipation by 2-3 orders of magnitude compared to saturation mode operation [Urazhdin 2002].

The schematic of the cryogenic charge sensor circuit is shown in Figure 18. It consists of two HEMTs. The one on the right is the measurement transistor. The gate of the measurement transistor is biased through the HEMT on the left. The bias HEMT simply acts as a very high resistor, preventing the charge induced on the tip from going to the left. The standard capacitor C_S is used to subtract away the stray capacitance, arising mostly out of the electric fields from the 2DES not terminating at the very apex of the tip. This is accomplished by applying an AC excitation to C_S, of almost the same amplitude but exactly 180^0 out of phase with the applied sample excitation.

The cross-sectional structure of a HEMT is shown in Figure 19. The epilayers consisting of undoped GaAs, Si-doped n-type $Al_xGa_{1-x}As$ and n-type GaAs are grown on a (100) semi-insulating GaAs substrate by molecular-beam epitaxy (MBE). Some epilayers are grown with a 6 nm-thick undoped $AlxGa_{1-x}As$ spacer layer inserted between the undoped GaAs and n-$Al_xGa_{1-x}As$ layers to enhance electron mobility. The AlAs mole fraction, denoted as x, is usually about 0.3.

The input capacitance C_{in} is the capacitance between the gate and the source-drain channel of the HEMTs. It is very important to have a small C_{in}, since the voltage measured by the lock-in amplifier V_{meas} is given by $V_{meas} = GV_{in}\frac{C_{meas}}{C_{in}}$. G is the gain of the circuit, which is usually ~1, V_{in} is the input voltage, which in our case is 8mV, and C_{meas} and C_{in} are the measured and input capacitance respectively. Thus low input capacitance means higher sensitivity. The input capacitance of the HEMT is 0.3pF

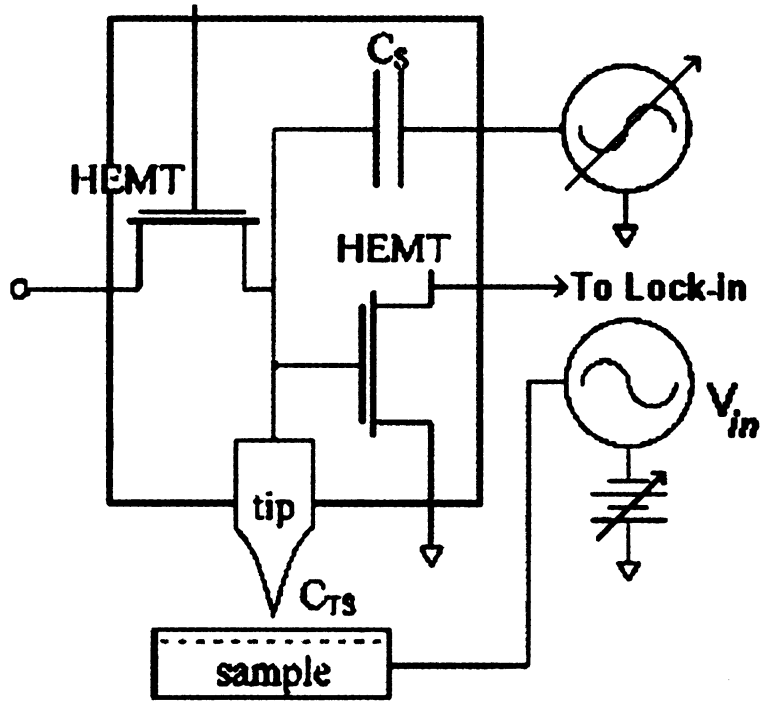

Figure 18. The cryogenic charge sensor circuit. C_{TS} is the tip-sample capacitance, C_S is the standard capacitor and V_{in} is the rms value of the applied AC excitation to the sample.

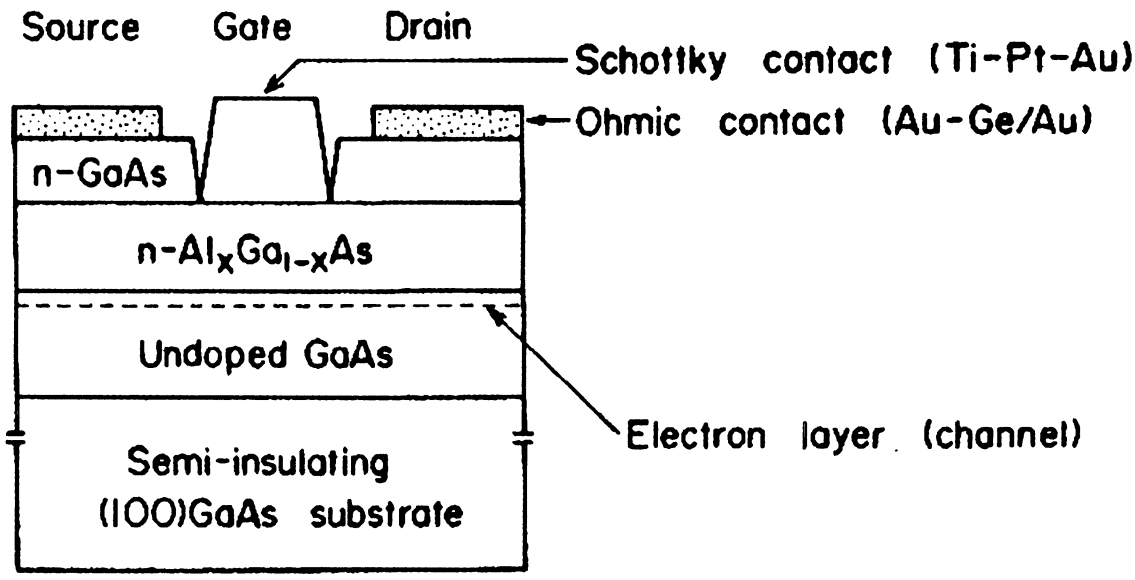

Figure 19. Typical cross section of a HEMT [Mimura].

ultimately allowing a charge sensitivity of 0.01 electrons/√Hz. The charge sensitivity number comes from the Johnson noise. If C_{in} is too large, V_{meas} is reduced and other sources of noise will dominate. This will lead to a decrease in the sensitivity. The drain current –voltage characteristic curves for different gate voltages of a typical HEMT are shown in Figure 20. Before we start our experiment, we look for the characteristic fan-shaped family of curves for our measurement HEMT on a curve tracer, to make sure the HEMT is working.

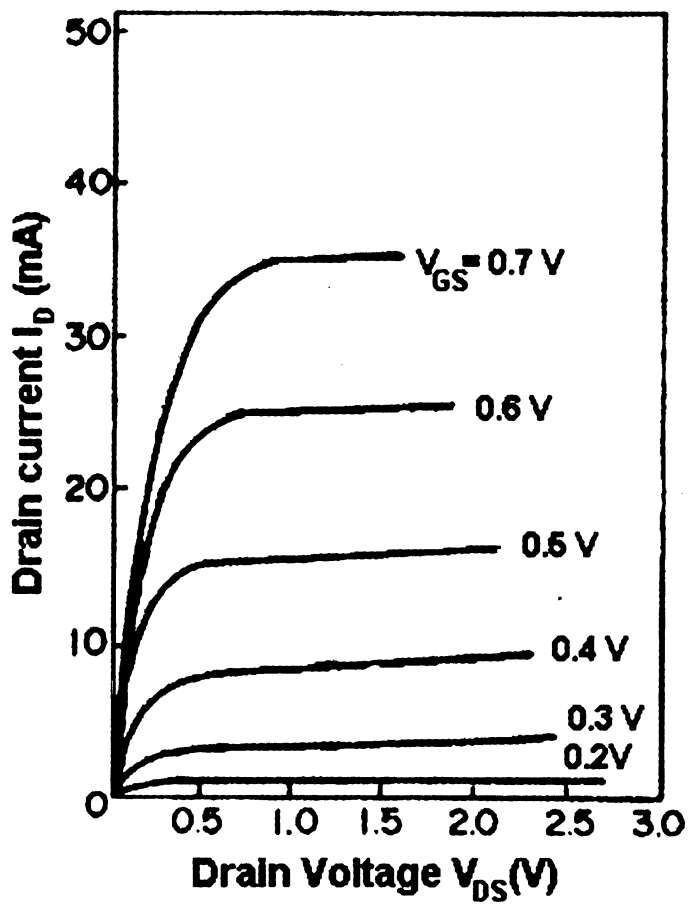

Figure 20. Drain current- voltage characteristics, at different gate voltages V_{GS}, of a typical HEMT [Mimura].

3.4 The cryostat

The scan head with the sensor chip and the sample is attached to the end of a long stainless steel stick. The stick is then mounted on a top loading He3 cryostat, and is inserted slowly into the cryostat. The cryostat has a superconducting solenoid surrounding the sample space, with which a magnetic field up to 12 T can be achieved. The arrangement is shown schematically in Figure 21. The operation of the He3 cryostat will be described briefly in this section.

The principle of a He3 cryostat is very simple. Gaseous He3 is liquefied and is pumped upon to reach the base temperature of 270mK. The whole cryostat is cooled in stages from room temperature to liquid He4 temperature of 4.2K. It is usually maintained at this temperature for months, by filling it up with liquid He4. The procedure for cooling down from 4.2K to the base temperature is as follows. Just outside the sample space and attached to its outer wall is a small pot called the 1K pot. The 1K pot is filled with liquid He4 and pumped upon to maintain it at around 1.2K. The He3 stored in a storage cylinder in gaseous form is allowed to enter the sample space, and starts to liquefy around the 1K pot and drips down into the bottom of the sample space. The sample space has a big charcoal adsorption pump, also called the sorb, which starts pumping on liquid He3, when the adsorption pump is below 10K. It is usually maintained at around 5K by using a He4 heat exchanger. The base temperature of 270mK is reached by pumping on the liquid He3 by the adsorption pump. The sample space remains at the base temperature for about 96 hours, until it runs out of liquid He3. At this point virtually all the He3 molecules are stuck to the adsorption pump, but they are recycled for subsequent data runs.

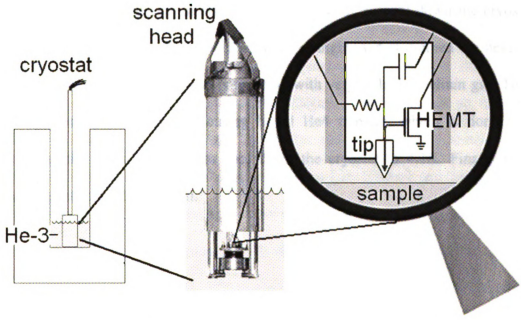

Figure 21. The top loading He3 cryostat with the microscope directly immersed in liquid He3. The microscope with the sample and the sensor chip is attached to a long stainless steel stick, which is used to insert the microscope inside the cryostat.

Inevitably the cryostat is allowed to warm up to room temperature from time to time. It must then be re-cooled from room temperature to 4.2K in an efficient way. The procedure for doing so is as follows. The cryostat has an outer vacuum chamber, which is first pumped down to pressures of 2-3 x 10^{-6} torr, and remains under vacuum throughout the cryostat operation. The cryostat also has another vacuum chamber called the inner vacuum chamber (IVC), between the main bath, which holds the liquid He4, and the sample space where the microscope is inserted. It is first evacuated of air and a tiny bit of dry nitrogen gas is introduced, to act as an exchange gas for the cool down. Liquid nitrogen is transferred very slowly into the main bath, to cool down the cryostat along with the magnet to 77K. The liquid is kept overnight, and is drained the next day. The IVC is evacuated once again and is filled up with very little dry helium gas. The helium gas acts as an exchange gas during liquid He4 transfer, which is done right after removing the liquid nitrogen, to cool down the cryostat to 4.2K. Finally the IVC is evacuated to 2-3 x 10^{-6} as well.

Chapter 4

Imaging disorder in a 2DES

The integer quantum Hall effects (IQHEs) [Prange, von Klitzing] and the fractional quantum Hall effects (FQHEs) [Tsui, Laughlin1983] are among the most remarkable phenomena to be discovered in solid-state physics in the last two decades. It is well known that disorder plays a major role in the formation of localized states in the Landau levels (LLs), the existence of which is ultimately responsible for the quantum Hall plateaus. Disorder in the GaAs heterostructures is due mostly to the randomly situated ionized donor atoms between the quantum well and the surface. Studying disorder in the two dimensional electron systems (2DES) is thus an important step towards understanding the quantum Hall states and other exciting phenomena such as metal-insulator transitions [Das Sarma], skyrmions [Das Sarma], and the predicted charge density waves (CDWs) [Koulakov, Moessner]. We use the charge accumulation imaging technique, to image the potential due to the random distribution of the ionized donor atoms at zero magnetic field. We observe micron-scale features, consistent with the previous work of Tessmer *et al* [Tessmer 1998] and Finkelstein *et al* [Finkelstein].

4.1 The simplest measurement

The simplest measurement that can be performed with the CAI technique is shown in Figure 22. Until now we have assumed implicitly that the tip is only a measurement device, and we do the capacitance measurements non-invasively. But we can also study how the tip can perturb the 2DES locally by applying a DC bias voltage.

Figure 22 shows the tip-2DES in-phase capacitance signal Q_{in} as a function of the DC tip voltage V_{tip} at a temperature of 290mK. In this measurement, the tip was fixed over a certain place in the sample, and its DC voltage was varied while the corresponding in-phase capacitance was measured. The capacitance curve shows a clear step feature. The step feature can be easily explained. Initially when V_{tip} is positive, the capacitance measured is between the tip and the fully charged 2DES, which is the case at the right side of the plot in Figure 22. As we decrease the tip voltage, it starts depleting the 2DES. At around a tip-voltage of ~ -0.25V the 2DES is completely depleted, and the signal drops abruptly, forming the step. The measured capacitance now is that between the tip and the 3D metallic substrate. Thus the 12aF step height is the difference in capacitance between a fully charged 2DES layer and the tip, and the back electrode and the tip – where the 2DES is locally depleted. As we decrease the tip bias voltage further the depleted hole in the 2DES grows in size. The voltage V_{null} shown in the plot is the work function difference between the tip material, which is an alloy of platinum and iridium, and the GaAs sample – called the contact potential. It is determined by a technique called the Kelvin probe method. We set $V_{tip}= V_{null}$ when we want to acquire data non-invasively.

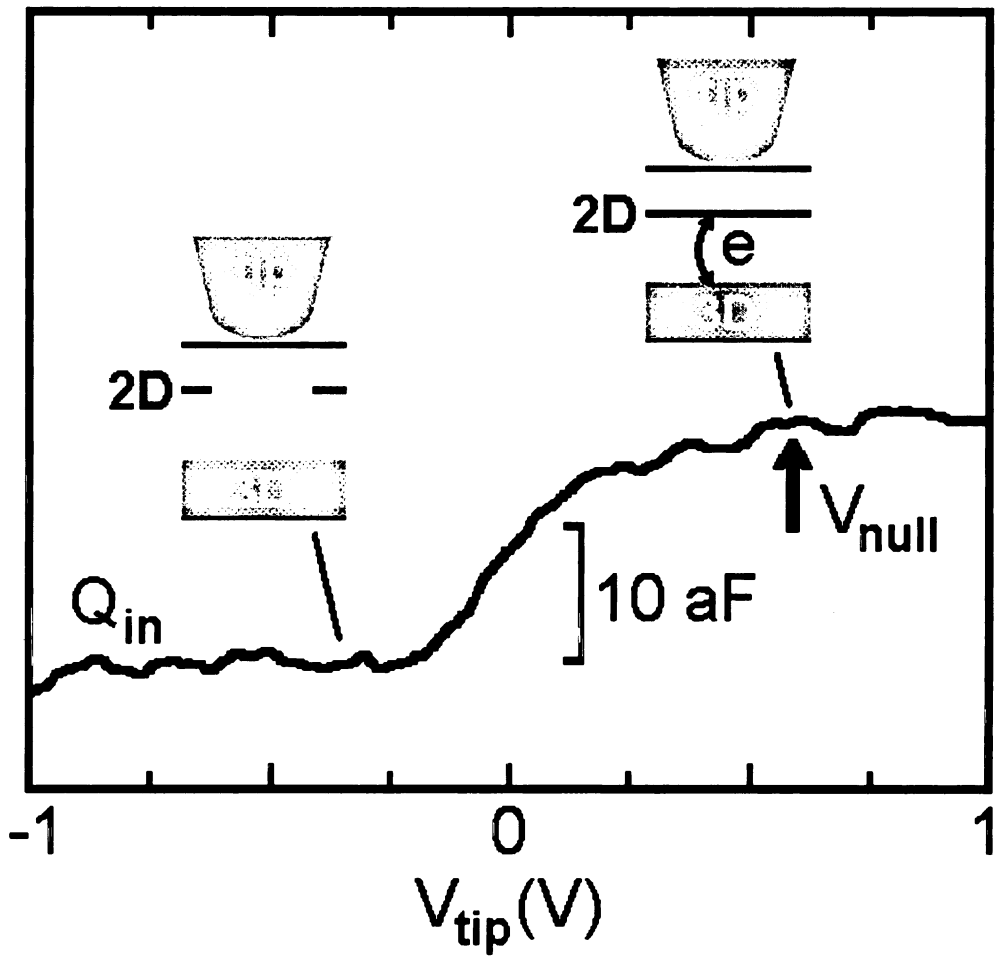

Figure 22. Dependence of the in-phase capacitance signal Q_{in} on the tip dc bias voltage. The step feature of approximately 12aF marks the potential where the 2DES becomes depleted locally. The data were acquired at 290mK.

4.2 Imaging disorder

While describing the sample in Chapter 2, it was mentioned that the donor atoms in the AlGaAs give up their electrons, which migrated to the quantum well to form the 2DES. Although the modulation doping technique reduces the scattering, the ionized donors still cause disorder within the 2DES. Also in the quantum Hall regime, the width of the Landau levels comes from the fluctuations of the density of charged donors. Hence it is very important to know the distribution of these charged donor atoms in the dopant layer in AlGaAs.

We would like to image the disorder potential due to these ionized donors [Chakraborty]. To test that CAI works in imaging this potential, we can intentionally introduce disorder by rearranging the ionized donors at a certain place in the sample. Figure 23 shows the image of such a place. The disorder was introduced by applying a large negative voltage (~ -10V) to the tip when it was very close to the sample. The large negative voltage rearranges the charge among the ionized donors in the dopant layer, so that the positively charged ions are accumulated below the apex and the surrounding region of the tip. The large voltage was then removed, and the image was obtained by scanning the tip over the sample at zero effective potential ($V_{tip}=V_{null}$). The lighter region in the image corresponds to greater electron accumulation. Therefore as evident from the figure, there was electron accumulation in the 2DES below the region where we introduced the excess positive charge. This data was taken at 290 mK.

Now to image the intrinsic disorder potential we scan the tip while the tip is depleting the 2DES. Also, we move to a different location away from the region where

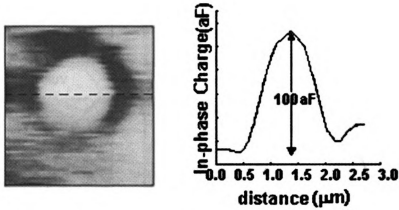

Figure 23. (a) A 3μm x 3μm image of an intentionally created disorder to test the CAI technique in imaging disorder. Bright regions imply greater electron accumulation. (b) A line scan through the disk of electron accumulation shows the capacitance at the center of the bright disk is approximately 100 aF more than the dark surrounding area.

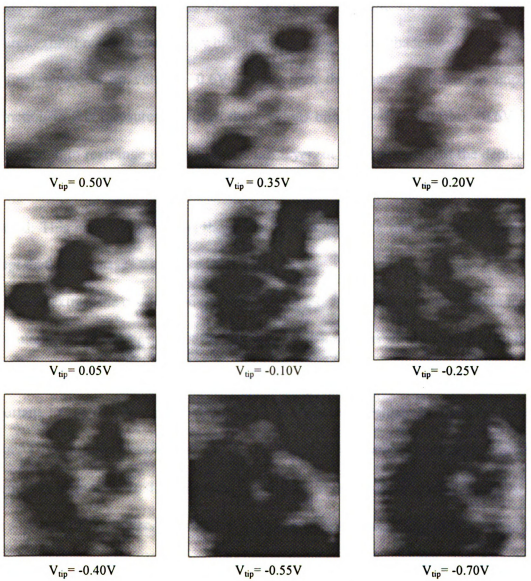

Figure 24. A series of 3μm x 3μm images with decreasing dc tip bias voltage starting from 0.5V, which is approximately equal to V_{null}, to –0.6V in decrements of 0.15. The features coalesce and the images get darker as the tip depletes the 2DES. The difference in capacitance from the brightest to the darkest region is approximately 500aF.

we intentionally introduced disorder. The scan images are shown in Figure 24. We start with the tip at 0.5V, and we make the tip voltage more and more negative with every scan image. As can be seen from the figures, the tip depletes the 2DES. The micron size features exhibit reduced charging, which is displayed as darker shades and coalesce. Thus the final image at tip voltage –0.6V is very dark throughout. There is an important distinction in this measurement from the previous one, which is that, this –0.6V is not large enough to rearrange charge in the donor layer. In this measurement the depletion is indeed caused only by the tip. A depleted "bubble" follows below the tip's apex as it is scanned. This experiment then is the scanning version of the data shown in Figure 22, except that these images were taken at about 1 ^{o}K.

In order to extract the distribution of the ionized donors, we need to process these images. Particularly, we need to get rid of the topography contribution which couples with the in-phase charging Q_{in}, but has nothing to do with the signal from the 2DES. Also it is important to set the gray scale to highlight the relative changes in charging for each image. The former was achieved by subtracting the image containing the most topography from the rest. The image that would have the most topography is easy to find. The structure in the image for which $V_{tip}=V_{null}$ should be exclusively due to topography, and hence we can consider this to represent the purely topographical contribution. In this case, the topographic image is the very first image in Figure 24, for which the V_{tip}= 0.5V. The latter was done by line-by-line averaging. Line-by-line averaging means shifting each line of an image so that its average value is zero. Naturally the average value of the entire scan is also zero, so that we have removed the offset due to the depleting voltage.

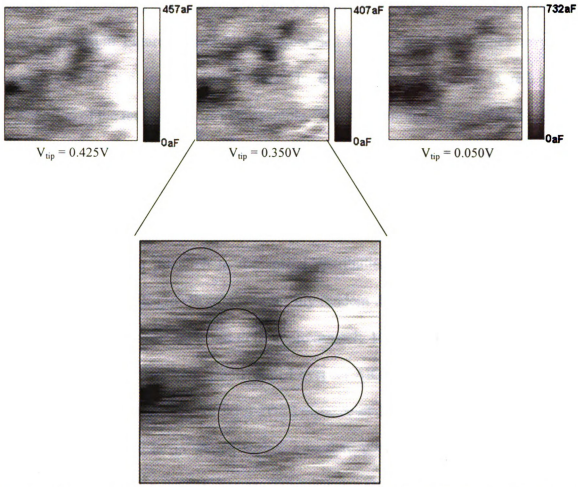

Figure 25. A series of 3μm x 3μm images processed from images in figure 24. Topographical contribution has been subtracted. The images show intriguing micron-scale features. The middle image is enlarged, and the micron-scale features are shown with circles in the enlarged image.

Moreover, this line-by-line subtraction serves to correct for tip-sample drift effects. The result is shown in Figure 25. Not all the processed images are shown since they are mostly similar. We interpret the features in these processed images to reflect the distribution of the ionized donors in the sample. The most intriguing part of the images is the micron-size features. According to theorists [Efros 1988, Efros 1999, Shklovskii], the amplitude of potential fluctuations in the donor layer is expected to vary as the square root of the donor density, and is assumed to be no larger than the donor layer-2DES distance. Turning our attention to the spatial distribution of the donors, it is widely believed that the MBE growth results in a truly random distribution. The average inter-donor distance in our case turns out to be approximately 10 nm, which is calculated from the dopant density of 10^{18} cm^{-3}, bulk doped over an AlGaAs thickness of 10 nm. This number is smaller than the donor layer-2DES distance of 20 nm, which is the key length scale. With regard to larger length scales, a random distribution means that all other length scales larger than the donor layer-2DES distance should be equally present. Hence present theories do not explain any mechanism that would lead to the distribution of ionized donors into these micron-sized islands. Tessmer *et al* [Tessmer 1998] and Finkelstein *et al* [Finkelstein] have observed similar micron-scale features using a technique, which employed a magnetic field to put the 2DES near integer filling. In their paper Finkelstein *et al* argue that screening by residual electrons in the donor layer smoothes the potential to micron lengths. But, any screening that might be present due to residual electrons in the donor layer should preferentially smooth out the larger length scales rather than the smaller ones. Hence we do not believe screening actually explains the micron length scales. It is possible that the micron-scale length scale is somehow tied

with the growth mechanism, although existing theories predict otherwise [Efros 1988, Efros 1999, Shklovskii].

Chapter 5

Charge Density Waves: Theory and Experiment

Two-dimensional electron systems formed in GaAs/AlGaAs heterostructures represent an ideal laboratory to study many-particle physics in lower dimensions. Under various conditions, electron-electron interactions may result in ordered inhomogeneous states. The Wigner crystal represents a classic example, arising from direct Coulomb repulsion at sufficiently low density, temperature, and disorder. In an applied perpendicular magnetic field, more general charge density wave (CDW) [Koulakov] ground states are possible. At sufficiently high Landau level filling, Hartree-Fock based theories predict a CDW ground state of length scale on the order of the cyclotron radius, resulting from the competition between Coulomb repulsion and exchange attraction [Koulakov, Moessner]. Recent transport measurements of high-mobility samples show that highly anisotropic dissipation occurs for more than four filled spin-split Landau levels, with the uppermost level near half filling [Lilly]. Unidirectional CDW stripes are believed to lie at the heart of these observations. In contrast to transport measurements, scanned probe techniques sensitive to electric fields can provide direct images of the GaAs/AlGaAs electronic structure. In this Chapter, I shall present a detailed theory of the formation of the CDWs, and discuss our effort in trying to resolve them with our CAI technique.

5.1 Theory of CDWs

Prior to 1982, physicists believed that the ground state of the 2DES in a perpendicular magnetic field was that of charge density waves (CDWs). But with the

discovery of the fractional quantum Hall effect (FQHE), the CDW picture, which does not exhibit FQHE, was replaced by the ad hoc Laughlin liquid picture at the lowest Landau levels (N=0,1). Laughlin liquid [Laughlin 1983] is a uniform incompressible quantum state. In the 1990s it became increasingly evident, both from calculations and experiments, that FQHE was absent for N>1. In 1996, Koulakov, Fogler, Shklovskii [Koulakov, Fogler 1996] and Moessner and Chalker [Moessner] independently proposed an alternative to the Laughlin liquid picture. The Laughlin liquid ground state was still lower in energy than the conventional Wigner crystal [Wigner] for N >1. But Koulakov, Fogler, Shklovskii, based on Hatree-Fock calculations, predicted that the ground state of a couple of CDW phases do actually have lower energies than the Laughlin liquid ground state for N >1. There has been a growing body of experimental evidence [Cooper, Lilly], albeit indirect, for the existence of at least one of the two predicted CDW phases. In the next few paragraphs, I shall present the essential elements of this CDW picture and show that for N >1 CDWs do win over the Laughlin liquid and Wigner crystal.

Before we begin let us define some of the important length scales and parameters. For a 2DES in a perpendicular magnetic field B, the spatial extent of the wavefunction of an electron is of the order of the magnetic length $\ell = \sqrt{\frac{\hbar}{eB}}$. Another relevant length scale is the classical cyclotron radius R_C given by $k_F\ \ell^2$, where k_F is the Fermi wave vector. Other parameters of importance are $\nu_N = \nu - 2N$, where ν is the spin-split filling factor, and N is the number of completely filled Landau levels. The factor 2 comes from the spin splitting of the Landau levels.

Assuming Wigner crystal (WC) [Wigner] to be the ground state of the 2DES in a perpendicular magnetic field, one can calculate the cohesive energy of the WC for the case when ν_N is not too small ($\nu_N >> 1/N$), i.e., when the cyclotron orbits at neighboring lattice sites may overlap. For the case when ν_N is indeed small, the concept of WC is natural. Cohesive energy is defined as the energy per particle at the upper Landau level with respect to that in the uncorrelated electron liquid (UEL) of the same density. The WC cohesive energy for not too small ν_N is given by [Koulakov]

$$E_{coh}^{WC} = -\frac{\hbar\omega_c}{16\pi N}\left[\frac{\sqrt{2}}{r_s} + \frac{3}{2\pi}\ln(N\nu_N)\right] - \frac{1-\nu_N}{2}\hbar\omega_c\frac{\ln(Nr_s)}{2N+1}. \qquad (5.1)$$

The factor r_s is defined by $r_s = \sqrt{2}/k_F a_B$, where a_B is the effective Bohr radius. In realistic samples $r_s \sim 1$. Let us now compare the cohesive energy of the CDW state, in the same regime, i.e., for $\nu_N >> 1/N$. It is given by [Koulakov]

$$E_{coh}^{CDW} \approx -f(\nu_N) r_s \hbar\omega_c \ln\left(1+\frac{0.3}{r_s}\right) - \frac{1-\nu_N}{2}\hbar\omega_c\frac{\ln(Nr_s)}{2N+1}. \qquad (5.2)$$

The function $f(\nu_N)$ is proportional to ν_N for $1/N << \nu_N << ½$. The second term in both cases is the same, and one has only to compare the first terms. So in the regime when $\nu_N >> 1/N$, the first term for the CDW case is more negative than the WC case and thus the CDW state has lower energy and wins over the WC state. The plot in Figure 26 shows the qualitative behavior of the WC and the CDW energies. Only the first terms of the equations (5.1) and (5.2) are plotted in units of $\hbar\omega_c$. The plot shows the transition of the system from WC to CDW phase. Here we have used $f(\nu_N) = 0.15\nu_N$, N = 5 and $r_s = 1$.

For the Laughlin liquid state, comparing the cohesive energy with the CDW state, it is not very obvious from the expressions that the CDW state wins over the Laughlin

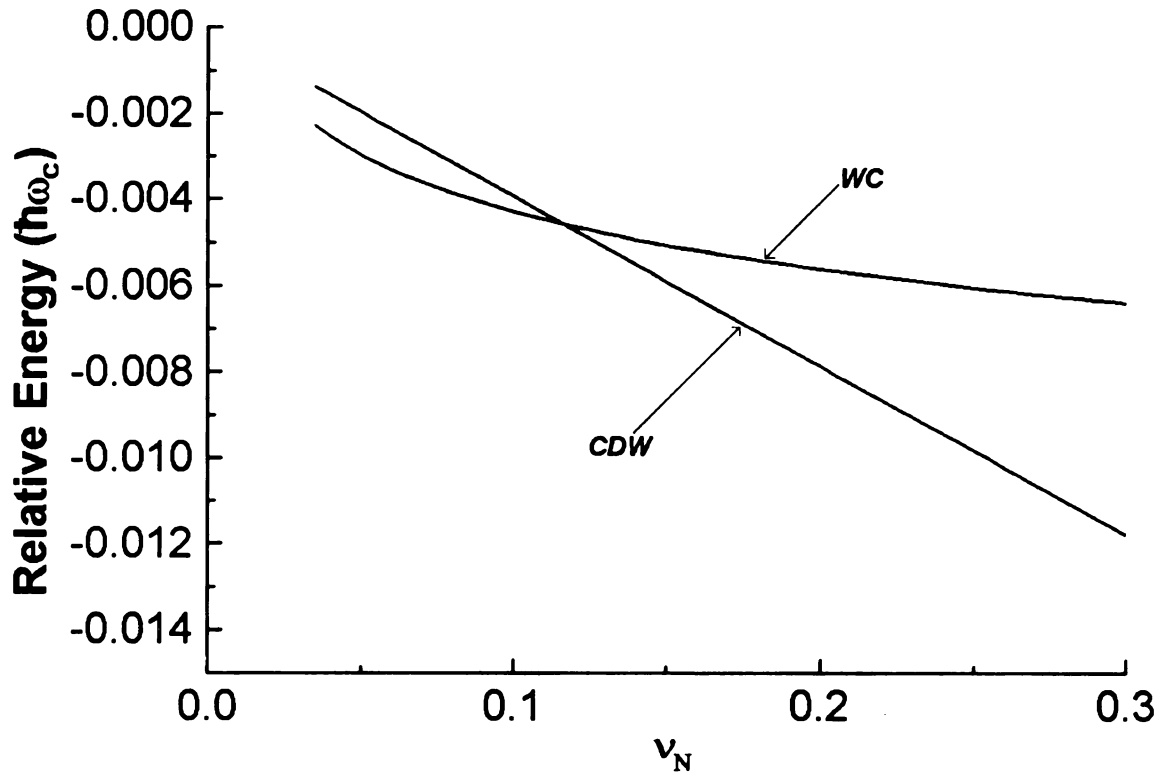

Figure 26. Plot of relative energies (only first terms in equations (5.1) and (5.2)) of Wigner crystal (WC) and charge density waves (CDW) in units of $\hbar\omega_c$ against ν_N. In this example, for approximately $\nu_N > 0.1$ the CDW has lower energy than WC.

state for N > 1. But the cohesive energies can be calculated numerically, and in the following table we present the results for $r_s = \sqrt{2}$. From the table one can see that for ν_N = 1/3 and N = 0 and 1, the Laughlin liquid is lower in energy. However for N > 1 CDW wins. The same is true for ν_N = 1/5 and N > 2.

$\nu_N = 1/3$					
N	$\tilde{M}$	E^{UEL}	E^{L}_{coh}	E^{CDW}_{coh}	$\delta E/E^{CDW}_{coh}$
0	1	−0.1206	−0.1159(1)	−0.1037	−11.8%
1	1	−0.1297	−0.1519(3)	−0.1424	−6.7%
2	2	−0.1136	−0.1141(3)	−0.1188	4.0%
3	3	−0.1034	−0.0946(3)	−0.1018	7.1%
4	4	−0.0965	−0.0824(3)	−0.0896	8.0%
5	5	−0.0914	−0.0733(3)	−0.0805	8.9%
$\nu_N = 1/5$					
N	$\tilde{M}$	E^{UEL}	E^{L}_{coh}	E^{CDW}_{coh}	$\delta E/E^{CDW}_{coh}$
0	1	−0.0560	−0.0903(2)	−0.0880	−2.6%
1	1	−0.0765	−0.1727(7)	−0.1692	−2.1%
2	1	−0.0677	−0.1420(9)	−0.1396	−1.7%
3	2	−0.0618	−0.1139(9)	−0.1202	5.2%
4	2	−0.0577	−0.0963(9)	−0.1050	8.3%
5	3	−0.0547	−0.0849(9)	−0.0946	10.3%

Table 1. The cohesive energies of the Laughlin liquid E^{L}_{coh} and the CDW E^{CDW}_{coh} for $r_s = \sqrt{2}$. $\tilde{M}$ is the optimal number of electrons per CDW bubble given approximately by $3\nu_N N$. The energy unit is $\hbar\omega_C$. The energy per electron in the uniform uncorrelated state E^{UEL} is also provided for reference [Fogler 1997].

Having established theoretically that CDW states for higher Landau levels (N >1) are preferred, let us try to understand the physics intuitively. It was briefly discussed in Chapter 1 (Section 1.2) that there was a competition between the long-range Coulomb repulsion and short-range ($\sim \ell$) exchange attraction between the electrons, which led to

the formation of clusters of electrons, called "bubbles" and "stripes" with a periodicity of ~$3R_C$. But this does not answer the question of why there is no CDW for low Landau level filling (N = 0 and 1). The answer lies in the all important length scale R_C, the cyclotron radius, which appears in the exponent of the CDW wavefunction. The wavefunction of a single bubble with M electrons at the lowest Landau level is given by

$$\Psi_0\{r_k\} = \prod_{i<j}(z_i - z_j) \times \exp\left(-\sum_{i=1}^{M} k_F \frac{|z_i|^2}{4R_C}\right). \tag{5.3}$$

Here $z_j = x_j + iy_j$ is the complex co-ordinate of the *jth* electron. The wavefunction of a bubble at the Nth Landau level centered at R can be constructed from the above wavefunction as

$$\Psi\{r_k\} = \prod_{i=1}^{M} \frac{(a_i^+)^N}{\sqrt{N!}} \exp\left(\frac{b_i^+ \overline{R} - b_i R}{\ell\sqrt{2}}\right) \Psi_0\{r_k\}, \tag{5.4}$$

where $a_i^\dagger$ is the inter-ladder operator, raising the *ith* electron to the next Landau level, and $b_i^\dagger$ is the intra-ladder operator. Finally, the wavefunction of the CDW, with an anti-symmetric combination of bubbles centered at the triangular lattice sites R_l is given by,

$$\Psi_{CDW} = \sum_P \mathrm{sgn}(P) \prod_l \Psi_l\{P(r_k)\}. \tag{5.5}$$

P's are the permutations of electrons between bubbles.

The intuitive reason for the absence of CDW for low Landau level filling (N = 0 and 1) is as follows. In all these arguments we are talking only about electrons in the upper partially filled Landau level. Laughlin liquid can be thought of as CDW state melted by zero point vibrations. The melting can occur only if the amplitude of the zero point vibrations is comparable to the lattice constant. This amplitude never exceeds the magnetic length ℓ. There is an important difference between low and high Landau level

filling. At low Landau level filling, Coulomb repulsion dominates, and the electrons can lower their energy by staying as far apart as possible. Hence the CDW contains only one electron per unit cell. The lattice constant is of the order of R_c, and it is small at low Landau level filling, since R_c is inversely proportional to the field. The lattice constant decreases with increasing filling factor, since now the system accommodates more electrons in the same amount of space. At some value of ν_N, the lattice constant becomes of the order of ℓ, the spatial extent of the electron wavefunction in a perpendicular magnetic field, and the crystal melts into a Laughlin liquid. At higher Landau level filling though, increasing the filling factor, adds more electrons to the lattice sites of the CDW crystal, so that the lattice constant does not change much. The lattice constant, which is of the order of R_C, is much greater than ℓ, at higher Landau level filling. Therefore it is unlikely that at higher Landau level filling the CDW would be melted by the zero point fluctuations.

The CDW state in equation (5.5) forms patterns shown in Figure 27. Each black dot in the figure represents the guiding center of the cyclotron orbits. An enlarged view of a "bubble" is shown in Figure 27(c). The dark region is the guiding centers of the cyclotron orbits of the electrons in the bubble, while the toroid is the charge density distribution. The aggregation of many particles into large domains helps the system achieve a lower value of the exchange energy, while the Coulomb repulsion keeps the aggregates separate. The actual charge density variation of the uppermost Landau level is of the order of 20%. At higher Landau level filling, when the system is very close to integer filling ($\nu_N \sim 1/N$), each bubble consists of one electron. As we move away from integer filling more electrons are added to the lattice sites forming the bubbles. This

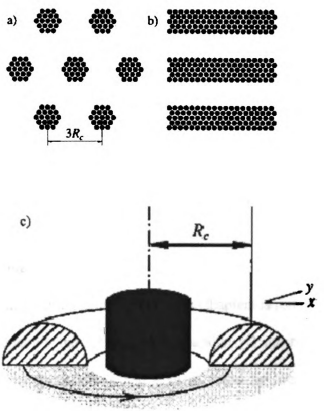

Figure 27. (a) "Bubbles". (b) "Stripes". The black dots are the guiding centers of the cyclotron orbits. The periodicity is ~ 3 R_C. (c) The enlarged quasi-classical image of a single bubble. The dark region is the guiding center of cyclotron orbits and the toroid is the charge density distribution, which is created by electrons moving in the cyclotron orbits centered inside the bubble. [Fogler 1997, Fogler 1996].

happens as long as $\nu_N < 0.3$. As the system moves further from integer filling, the bubbles coalesce to form the stripes.

The motivation for this experiment is to resolve these predicted bubbles and stripes. We have calculated the periodicity of these CDW structures, for the magnetic field we use and the density of our sample. The calculation goes as follows:

The periodicity of a CDW lattice according to prediction $\approx 3R_c$. $R_c = k_F \ell^2$, and k_F in 2D $= \sqrt{2\pi\rho} = 1.94 \times 10^8$ m^{-1} for 2DES density $\rho = 6 \times 10^{15}$ m^{-2}. While $\ell^2 = \frac{\hbar}{eB} = 1.64 \times 10^{-16}$ m^2 for magnetic field $B = 4$T. Hence $3R_c = 3 \times 1.94 \times 1.64 \times 10^{-8}$ m ≈ 95 nm, comparable to our spatial resolution of ~60 nm.

5.2 The CDW experiment

The measurement described in the previous Chapters is reiterated here as follows: A tunneling barrier separates the 2D layer and a parallel 3D substrate. An AC excitation voltage applied between the substrate and a sharp metal tip locally induces charge to tunnel back and forth between the 3D and 2D layers. A Schottky barrier blocks the charge from tunneling directly onto the tip. The measured signal is the resulting AC image charge on the tip electrode, which is proportional to the number of electric field lines terminating on it. In this way, the experiment provides a local measurement of the ability of the 2D system to accommodate additional electrons. The method can be considered as a locally resolved version of the pioneering work of Ashoori *et al.* [Ashoori 1990], and Eisenstein *et al.* (in a 2D-2D tunneling geometry) [Eisenstein], which demonstrated that the tunneling signal into a 2DES is sensitive to both gaps in the energy spectrum at integer Landau level fillings, and a Coulomb pseudogap that is pinned to the

Fermi level of the 2D system. At particular magnetic fields, we observe micron-scale features, corresponding to ordered electronic density modulations. To the best of our knowledge, these data represent the first tunneling images of the interior of a GaAs/AlGaAs 2DES.

The sample used for these measurements was an $Al_{0.3}$ $Ga_{0.7}As$ / GaAs (001) wafer grown by molecular beam epitaxy (MBE), discussed in Chapter 2. The average electron density in the 2DES is $6x10^{11}$ cm^{-2}, the low-temperature transport mobility is $\sim 10^5$ cm^2/Vs, and the zero magnetic field 3D-2D tunneling rate is approximately 200 kHz. Cryogenic temperatures are achieved by direct immersion in liquid helium-3 at 270mK. We position the tip to within a few nanometers of the sample surface using a scanning head discussed in Chapter 3 as well. The image charge signal is detected using a sensor circuit discussed in detail in Chapter 3. Most of the signal (~99.8%) corresponds to electric field emanating from areas macroscopically far from the location under the probe. We subtract away this background signal using a bridge circuit. To acquire images, the tip is scanned laterally across the surface without the use of feedback. We apply an excitation voltage of 8 mV rms at a frequency f=20 kHz. In addition, we apply a DC voltage of 0.6 V to the tip to compensate for the tip-sample contact potential, as measured *in situ* using the Kelvin probe technique [Tessmer 1998, Yoo]; hence the effective DC voltage is zero. The spatial resolution of the measurement is roughly 60 nm [Tessmer 2002], limited by the radius of curvature of the chemically etched PtIr tip (50 nm) and by the tip-2DES distance (60 nm). All images presented here were acquired and are displayed with identical sample orientation. To establish the technique's sensitivity to the 2D electron system, Figure 28(a) shows the measured charging as a function of

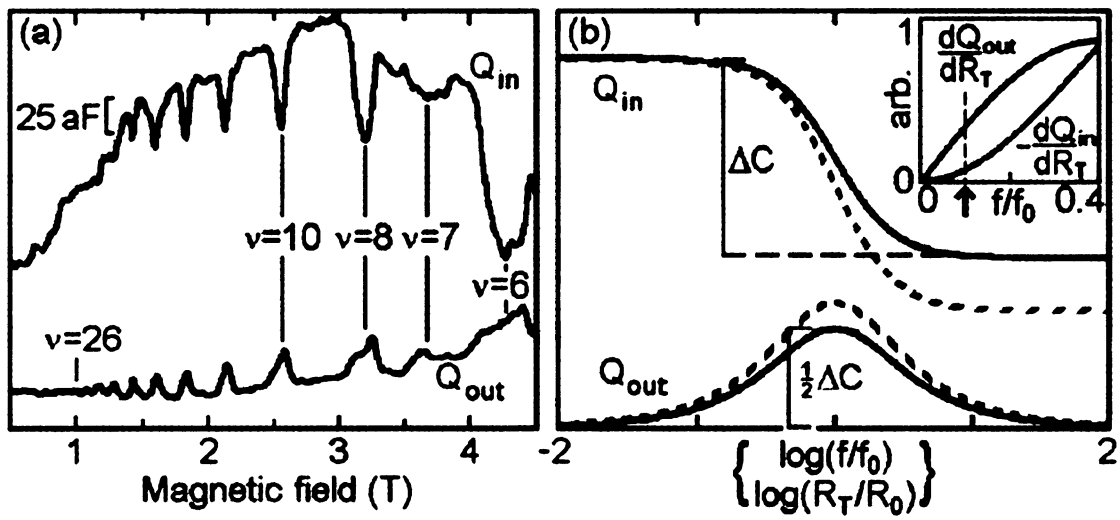

Figure 28. (a) Fixed-tip measurement. As a function of perpendicular magnetic field, Q_{in} and Q_{out} display clear features at integer Landau level filling ν. (b) Calculated in-phase and out-of-phase charging based on the equivalent circuit. Rigorous modeling for the system considers the distributed nature of the tip-sample capacitance and the effect of charge motion within the 2D plane. The dashed curves show qualitatively enhancements, which occur if the in-plane relaxation rates approach the tunneling rate, an effect that may occur near integer filling. (Inset) A linear plot of the derivatives of Q_{in} and Q_{out} with respect to tunneling resistance. In the low-frequency limit of this experiment (arrow), the out-of-phase component is more sensitive to R_{tun} variations [Maasilta 2003, Maasilta (rapids)].

magnetic field with the tip position fixed (i.e. not scanned), acquired using the same tip as for the subsequently displayed images. Both the in-phase and out-of-phase curves (acquired simultaneously) show clear structure with *1/B* periodicity, corresponding to integer Landau level fillings. To understand the origin of the in-phase dips and out-of-phase peaks, we invoke the charging characteristics of the model equivalent circuit described in detail in Chapter 3. Figure 28(b) plots the calculated variation of Q_{in} and Q_{out} with frequency f and resistance R_T. This is the same plot shown in Chapter 3, and is shown here again for convenience. The charging components have identical functional dependence on f and R_T, with characteristic values of $f_0=[2\pi R_T(C_T+Ctip)]^{-1}$ and $R_0=[2\pi f(C_T+Ctip)]^{-1}$, respectively. The magnitude of the curves is set by the tip-sample capacitance difference ΔC between a fully charging and locally non-charging 2DES. For the actual measurements, the characteristic zero magnetic field tunneling rate is f_0 ~200 kHz, a factor of ten greater than the applied excitation (i.e., f/f_0 ~0.1). Therefore we focus on the model's low-frequency behavior, $f/f_0<<1$; as shown in the inset, the out-of-phase component is more sensitive to variations in the local tunneling resistance. In contrast, the in-phase component is mostly sensitive to capacitance variations (not shown), including the compressibility contribution to the capacitance [Tessmer 2002, Smith]. In a parallel plate capacitor model, the measured capacitance is given by [Stern, Smith]

$$\frac{1}{C_{meas}} = \frac{1}{C_{geom}} + \frac{1}{e^2 \frac{dn}{d\mu}}. \qquad (5.6)$$

where C_{meas} is the measured capacitance and C_{geom} is the geometric capacitance. Hence, we conclude that the dips in the measured in-phase curve reflect a reduction in capacitance caused by the diminished compressibility $\frac{dn}{d\mu}$ of the 2D system at integer

filling. With respect to the out-of-phase curve, the peaks at integer filling likely reflect an increase of the pseudo gap, resulting in an increased tunneling resistance R_T [Deviatov]; variations in the in-plane conductivity may also contribute.

Figure 29(a) presents typical in-phase and out-of-phase charging images far from integer filling. The in-phase data are representative of hundreds of similar images which show charging patterns that are insensitive to magnetic field. We attribute this structure to surface topography, which modulates the geometric capacitance and couples preferentially to Q_{in}. This conclusion is supported by comparison to a surface topography measurement (at a different location) acquired by operating the microscope in a standard scanning tunneling microscopy mode [Urazhdin 2000]. As shown in Figure 29(b), the surface consists of elongated mounds qualitatively similar to the in-phase structure. These surface features point along the $[\bar{1}10]$direction, as indicated, reflecting an MBE growth anisotropy [Ballestad]. In contrast to the in-phase images, we find the out-of-phase images can show significant changes with magnetic field. The Q_{out} images also show features arising from surface topography, although this effect is significantly smaller than for the Q_{out} component (as expected in the low-frequency limit). For example, in Figure 29(a) the out-of-phase gray scale is an order of magnitude smaller than the in-phase scale. Because the in-phase component does not change significantly with field, we find that a convenient method to remove the small topographical contribution to Q_{out} is to scale down the corresponding Q_{in} image and then subtract it from Q_{out}. Figure 29(c) shows the same out-of-phase data as Figure 29(a), where we have subtracted the topography in this way. We see that in this case no significant features remain in Q_{out} discernible above the background noise, as was typical for the out-of-phase images far from integer filling. As

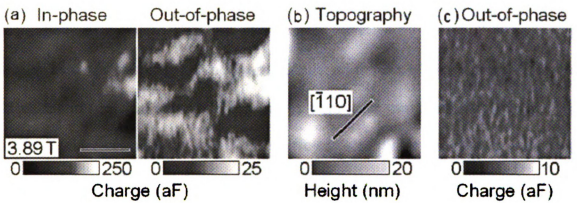

Figure 29. (a) Representative scanning images of Q_{in} (left) and Q_{out} (right) with an applied magnetic field far from integer filling of 3.89 T; scale bar length=1μm. (b) Topographical surface image showing the orientation of the growth features. The image was acquired at room temperature without altering the orientation of the crystal. The elongated mounds point along the $[\bar{1}10]$ direction, as indicated by the orientation of the scale bar, scale bar length= 2 μm. (c) Topography-subtracted out-of-phase image corresponding to the same data shown in (a). The images have been filtered to remove nanometer-scale scatter [Maasilta (rapids)].

the magnetic field approaches integer filling, while the Q_{in} images remain unchanged, the simultaneously acquired Q_{out} images show completely different behavior, clear and reproducible features appear that are not correlated with topography or experimental parameters such as scan direction.

Figure 30(a) shows a series of topography-subtracted Q_{out} images acquired sequentially near filling factor ν=6 at the fields indicated by the small arrows; very similar behavior was observed near ν=4. Similar to the out-of-phase peaks of Figure 28(a), the imaged Q_{out} structure likely results from local variations of the pseudo gap and/or in-plane conductivity. In either case, we can identify the structure as originating from modulations in the 2DES density ~5% which bring the system slightly closer and further from integer filling as a function of lateral position [Tessmer 2002]. Some of the Q_{out} features appear as randomly situated micron scale droplets, such as the bright feature in the upper right corner of the 4.38 T image. These are consistent with droplets and potential contours observed in references [Tessmer 1998] and [Finkelstein], which utilized direct ohmic contacts to the 2DES (i.e. non-tunneling experiments). Following this work, we interpret the droplets as originating from static density modulations induced by the disorder potential. This view is also supported by observations we have made of random features that reappear and evolve in a similar manner at successive integer fillings. In contrast to references [Tessmer 1998] and [Finkelstein], the images exhibit additional structures with orientational order, superimposed with the random droplets. To clearly demarcate these structures, we apply a standard approach based on the 2D Fourier transforms: $F(k_x,k_y)=\mathsf{F}[Q_{out}(x,y)]$, where k_x and k_y are the wave vector coordinates. The topography has been subtracted from the Q_{out} data as described above.

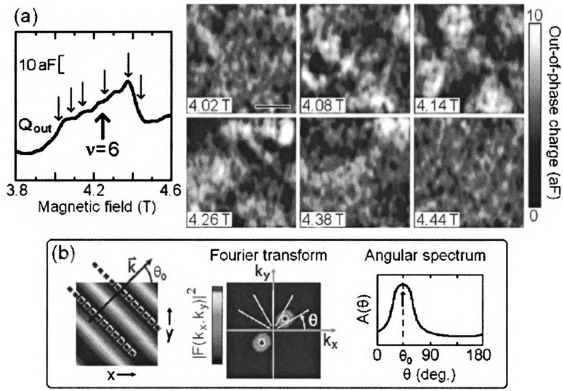

Figure 30. (a) Topography-subtracted out-of-phase data near six filled Landau levels. The fixed-tip curve to the left shows the ν=6 Q_{out} peak with arrows indicating the fields of the displayed scanning images. The displayed images have been filtered to remove nanometer scale scatter; scale bar length=2 μm. The crystal orientation is identical to Figures 29(a) and 29(b). (b) Schematic of Fourier analysis procedure to identify orientationally-ordered structure. The parallel lines in the direct image (indicated with dashes) can be described with wave vector $\vec{k}$, giving maxima in the Fourier transform power spectrum at $\pm\vec{k}$ (shown as black dots). The orientation of the wave vector θ_0 is seen as a peak in the angular spectrum, calculated by integrating the transform image along a series of radial lines at angle θ [Maasilta (rapids)].

Because we are interested in the spatial patterns and not the shift in the average value (this information is already given by the fixed-tip curves), we have subtracted a constant from each image to set the average value to zero. No additional processing or filtering was performed on the data prior to taking the Fourier transforms. To further emphasize orientational order, we have also calculated the angular spectrum $A(\theta)$ by integrating the Fourier power spectrum along radial lines oriented at angle θ, $A(\theta) = \int_{k_{min}}^{k_{max}} |F(k\cos\theta, k\sin\theta)|^2 \, dk$ as shown in Figure 30(b). The integration limits, k_{min} and k_{max}, set the range of wave vectors to be included; of course, they can be expressed in terms of cutoff wavelengths: $k_{min}=2\pi/\lambda_{max}$ and $k_{max}=2\pi/\lambda_{min}$. Figure 31(a) presents three sets of unfiltered Fourier transforms and angular spectra corresponding to Q_{out} images of Figure 30(a). We see that the transform at 4.14 T has developed clear maxima at relatively short wave vectors. To highlight the corresponding range of wavelengths, the angular spectra are calculated choosing cutoffs of $\lambda_{min}=1\mu m$ and $\lambda_{max}=3\mu m$, displayed directly below each transform image. We see that the 4.14 T angular spectrum shows the strongest structure at these short wave vectors; the prominent peak indicated by the arrow results directly from the maxima in the transform image.

Figure 31(b) compares the 4.14 T spectrum (near $\nu = 6$) to a similar observation obtained at a different location and at a field of 6.75 T (near $\nu = 4$). Figure 31(c) shows the corresponding Q_{out} images, where the arrows point to the stripe-like modulations that form the prominent peak in the angular spectra. As an example of the raw data, we also show the 6.75 T out-of-phase image with no filtering. These lines roughly point along the [110] direction. The images show evidence of weaker modulations in other directions. We have acquired dozens of Q_{out} images near $\nu = 6$ and $\nu = 4$ that show similar micron-

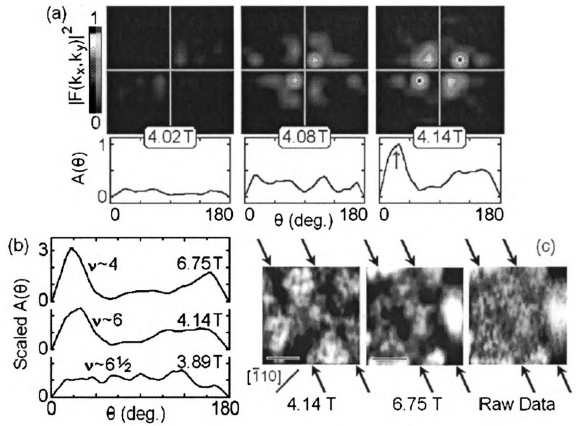

Figure 31. (a) Fourier power spectra and angular spectra corresponding to three Q_{out} images of Figure 30(a), normalized to the peak value at 4.14 T. The power spectra are displayed over the range ±6.67 μm^{-1}; the magnitude of the wave vector corresponding to the 4.14 T maxima is 2.4 μm^{-1}, or a wavelength of 2.6 μm. (b) Angular spectra from three different sample locations and magnetic fields. Similar peaks were observed near four (6.75 T) and six (4.14 T) filled Landau levels. For comparison, a spectrum far from integer filling (3.89 T, corresponding to Figure 29(c)) is included. In this plot, each curve is scaled to have an average value of 1.0, which serves to enhance the weak 3.89 T curve. The minimum at 0 and 180° is an experimental artifact arising from the scan direction. (c) The topography-subtracted Q_{out} images at 4.14 T and 6.75 T with arrows pointing to the structure that yields the prominent Fourier peaks. Also included is the 6.75 T data for which no filtering was applied. The [$\bar{1}$10] crystalline direction is indicated; scale bar length=2 μm [Maasilta (rapids)].

scale structure. In contrast to the droplet features that mirror static potential variations, the stripe-like structure appears to form spontaneously. Unlike the droplets, these structures shift position and evolve dramatically with magnetic field, as can be seen in Figure 30. The high sensitivity to magnetic field precludes tunneling barrier non-uniformity as the origin. In addition, we note that scanning tunneling microscopy and atomic force microscopy measurements show no evidence of atomic step edges oriented along [110]. We have not observed such structure near ν =5 nor ν =3. (The 10 T limit of our superconducting solenoid prevents probing Landau level fillings less than ν =3 for this sample.) We have not found evidence of ordered structure on the predicted cyclotron radius length scale, ~100 nm.

In summary, we have obtained the first direct images of ordered structure within the interior of a GaAs/AlGaAs 2DES using a novel scanned probe method. At magnetic fields near four and six filled Landau levels, we observe density modulations that exhibit clear orientational order, roughly along the [110] crystalline direction. The features are suggestive of micron-scale stripe-like states. However, because the spacing between features is a substantial fraction of the experimental scan range, we can only give a rough value for the characteristic length scale, and cannot speak to the periodicity of the structure. It is tempting to equate the observations with states similar to theoretical high-Landau-level charge density wave states [Koulakov] discussed in this Chapter. However, the length scales represent a major discrepancy: our calculations from theories predict a characteristic length set by the cyclotron radius ~100 nm, much smaller than the observed structures ~2 μm. It is possible that the physical origin of the modulations is similar to the CDW theories, but that disorder causes a larger length scale to be selected. Alternatively,

the structures may arise from an entirely different mechanism. Clearly, more theoretical work is needed.

Chapter 6

Quantum Dots

Quantum dots are small structures in solids containing electrons confined in all three directions [Kastner, Kouwenhoven 1997, Kouwenhoven 2001]. This confinement leads to discrete energy levels for the electrons, much like an atom. Although the confining potential in a quantum dot can be chosen at will, the one kind that will be studied in the present experiment is bowl-like or parabolic. In this Chapter we shall describe the theory of quantum dots confined by the parabolic potential, discuss the motivation behind the experiment and finally show some preliminary results.

6.1 Quantum dots: theory and motivation

Although quantum dots are very similar to real atoms in that they form discrete energy levels, there is one very important difference between them [Ashoori 1996]. The quantum dots are typically much larger in size than a real atom. The electron orbits of the dots do not scale in size. Imagine an atom containing many electrons whose size is continuously variable. As it is made larger the Coulomb energy due to repulsion between electrons orbiting around the nucleus decreases because the average spacing between the electrons increases. However, as the atomic size increases, the separation in energy of the different orbits of electrons decreases faster than the Coulomb energy. Hence in quantum dots the electrons are effectively much closer, and Coulomb interactions are much more significant than in a real atom. What all these mean is that although the two are very similar, and we have extensive knowledge about real atoms, quantum dots are very

interesting systems for studying basic quantum mechanics and electron-electron interactions.

Electronic states in quantum dots are described by their energy eigenvalues and corresponding eigenstates. The standard model for these dots assumes N electrons confined by a parabolic potential $\frac{1}{2}m^*\omega_0^2 r^2$ (m^* is the effective electron mass, ω_0 is the angular frequency and r is the radial distance) in a 2D plane interacting via Coulomb repulsion. In a perpendicular magnetic field the exact solutions for non-interacting electrons for the energy eigenvalues, with n, l, σ, being the radial, angular momentum and spin quantum numbers for the electrons are given by [Fock, Darwin]

$$E_{n,l,\sigma} = \hbar\sqrt{\left(\frac{\omega_c}{2}\right)^2 + \omega_0^2}\,(2n+|l|+1) - \frac{l\hbar\omega_c}{2} + g^*\mu_B B\sigma, \qquad (6.1)$$

$$n = 0, 1, 2 \text{ etc. } l = \pm 0, \pm 1, \pm 2 \text{ etc. and } \sigma = \pm\frac{1}{2}$$

where $\omega_c = \frac{eB}{m^*}$ is the cyclotron frequency, μ_B is the Bohr magneton, and g* is the effective g-factor. The eigenstates are given by [Maksym]

$$\Psi_{n,l}(r,\theta) = r^{|l|}\exp(-il\theta)L_n^{|l|}\left(\frac{r^2}{2a^2}\right)\exp\left(-\frac{r^2}{4a^2}\right), \qquad (6.2)$$

$$a^2 = \frac{\hbar}{m^*\sqrt{\omega_c^2 + 4\omega_0^2}}$$

where $L_n^{|l|}$ is a Laguerre polynomial. The quantum number n gives the number of nodes in the radial direction and l gives the number of nodes circumferentially.

This is a very simple picture and does not take into account the Coulomb interactions. Many observations can already be explained with this simple picture, by assuming the Coulomb interaction to be a small perturbation, so that the energy levels are the usual quantum levels due to the parabolic potential plus the additional Coulomb charging energy that varies smoothly with particle number. This picture accounts for the shell structure observed by Tarucha *et al* [Tarucha, 1996], which arises from the $(2n+|l|+1)$ factor in equation (6.1). Addition spectra also show transitions, which are not explained by this simple model but can still be understood in terms of single-particle levels subject to the exchange interaction. However a thorough understanding of the transitions requires precise calculations. Recent calculations [Tarucha, 1998] show deviations from the single-particle model. Although some indications of this structure may be present in the addition spectra results reported by Tarucha *et al* [Tarucha, 1996], a new technique capable of identifying these quantum states is needed.

Another important aspect is the interplay between disorder and electron-electron interactions in a quantum dot. The disorder would most likely distort the parabolic potential in a quantum dot into an irregular shape, leading to eigenstates much different from equation (6.2). Moreover the shape would depend on the exact location of the impurities and donor density variations. The interplay between disorder and electron-electron interactions can lead to remarkable behavior. For example in some cases electrons seem to be violating Coulomb repulsion, and two of them enter the dot at the same energy [Zhitenev 1997, Zhitenev 1999, Brodsky]. Most of the experiments done

until now have focused on the addition spectra of the system. With our CAI technique we will not only be able to study the addition spectra, but also CAI in principle has the profound capability to image the spatial characteristics of the quantum states and thus test both many-body effects and the effects of disorder on the eigenstates.

As shown in Figure 32, the same tunneling geometry that was employed to image the CDWs can be employed to image the wavefunctions of a quantum dot and to do spectroscopy of the dot. A gold gate is fabricated on the surface of the sample. By applying a negative potential to the gate, the 2DES is completely depleted, except in the hole region, which forms the quantum dot. By applying a negative voltage further, electrons can also be pushed from the dot region. While raising the gate voltage would add electrons to the dot, which would tunnel from the metallic substrate into the dot. With the tip fixed and varying the gate voltage, we can do spectroscopy of the dot, i.e., electrons will be added to the dot when the gate potential is equal to the energy level spacing, and would show up as enhanced capacitance (a peak in a capacitance versus gate voltage plot). On the other hand to image the amplitude of the wavefunction, we would scan the tip at a particular gate voltage that corresponds to a peak in the addition spectra.

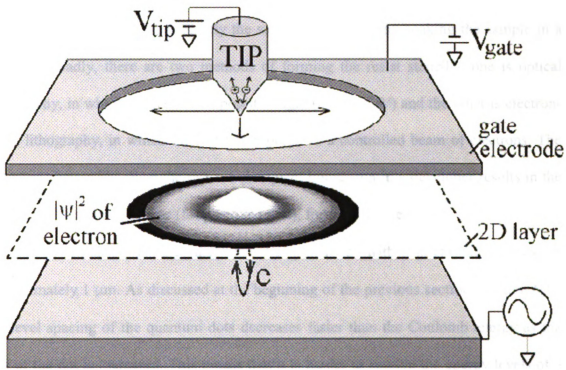

Figure 32. Schematic of wavefuntion imaging for a quantum dot. A single electron resonates between the bottom electrode and the dot. By mapping out the density variations, quantum wavefunctions can be probed. As an example a 3D plot of $|\psi|^2$ in the single-particle approximation is shown.

6.2 Quantum dot fabrication

To achieve lateral confinement of electrons in the 2DES we fabricate metallic gates on the surface of the sample. Application of a negative voltage on the gates depletes the 2DES of electrons below the gate region, leaving a confined puddle of electrons in the un-gated region. The method of fabricating the gates is quite similar to the ones used in the semiconductor industry. First a resist stencil of the pattern is made. Then the particular metal is deposited. Finally the stencil is removed by soaking the sample in a solvent. Broadly, there are two methods of forming the resist stencil – one is optical lithography, in which the resist is exposed to light (usually UV) and the other is electron-beam lithography, in which the resist is exposed to a controlled beam of electrons. The exposure chemically alters the resist. Subsequent immersion in a developer results in the removal of the exposed areas (for positive resist), forming the stencil.

The smallest feature that can be patterned with optical lithography is approximately 1 μm. As discussed at the beginning of the previous section (Section 6.1), the level spacing of the quantum dots decreases faster than the Coulomb energy as the size of the dot is increased. This means that it is harder to resolve the energy levels of a bigger dot compared to a smaller one. Hence one needs to fabricate small dots, and 1μm dots may not be small enough. Although it is possible to improve on the resolution of optical lithography, it is much easier to use electron-beam lithography, which can easily achieve resolutions of sub-100 nm. Ideally the resolution of e-beam lithography is limited by the beam diameter, which is typically 10 nm, but is extremely difficult to achieve in practice. In the following paragraph I shall describe the fabrication of the metallic gates with e-beam lithography.

Before the procedure can be started, it is very important to clean the surface of the sample of dirt and grease. For relatively clean substrate, ultrasonic cleaning in acetone, isopropyl alcohol (IPA) and de-ionized water in that order is sufficient. For a really dirty substrate, scrubbing with Alconox should be done first, before proceeding to acetone. The substrate is finally dried by blowing dry nitrogen gas. To aid the adhesion of the resist, the substrate may be treated with hexa-methyl disilizane (HMDS) vapor for 10-15 minutes, but this was not always done. The resists used to form the stencil in the e-beam process are based on methyl-merthacrylates (PMMA or MMA). The usual technique used to form a smooth layer is to spin the substrate rapidly while adding the liquid PMMA/MMA. A layer of PMMA/MMA 6% was spun on the sample at 3000 rpm for 50 seconds. It was then baked at 200 ^{0}C in an oven for an hour to remove the solvent and to harden the resist. This layer of resist can be exposed to a beam of electrons and developed. PMMA/MMA is a long chain polymer. When it is exposed to a beam of electrons, the polymer chain is broken. The coating is then dipped in a developer – which is generally a solution of MIBK (Methyl-iso-butyl Ketone) and IPA. The developer removes the exposed resist, to form the pattern as shown in Figure 33(b). The problem with this procedure is that when the metal is deposited, a thin layer of it tends to stick to the sidewalls of the resist and forms a continuous coating. This makes it very hard to lift-off the resist stencil.

One way to circumvent the problem is to spin another layer of a different resist on top of the 6% PMMA/MMA. A layer of PMMA 2% was thus spun at 4000 rpm for 50 seconds on top of the first layer. It was also baked in an oven at 200 ^{0}C for an hour to

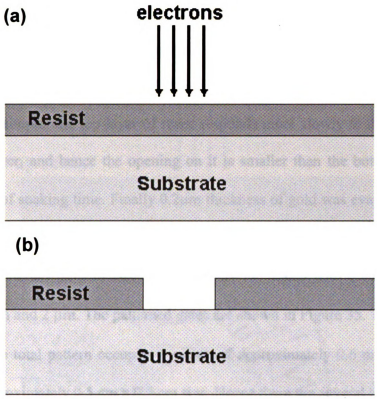

Figure 33. Single layer resist process. (a) The resist is exposed to a beam of electrons. (b) Resist after being exposed and developed.

remove its solvent and to harden it. It was then exposed to electron beam in a JEOL840 e-beam writer. The dose (defined as the amount of charge incident on an unit area of the sample) used was 250μC/cm^2 with a current of 20pA. What this does is produce an overhang of the top resist when developed, as shown in Figure 34(b). This overhang produces a natural break in the metal film during deposition. The reason the overhang forms is very simple: the top layer of resist responds more slowly to the developer than the bottom layer, and hence the opening on it is smaller than the bottom layer for the same amount of soaking time. Finally 0.2μm thickness of gold was evaporated and lifted off in acetone to produce the pattern shown in Figure 35.

Four different sizes of circular gates were fabricated with diameters of 0.5 μm, 1.0 μm, 1.5 μm and 2 μm. The patterned gates are shown in Figure 35. The line thickness is 0.2 μm. The total pattern occupies a square of approximately 0.6 mm x 0.6 mm in a sample of approximately 0.5 cm x 0.5 cm size. Hence there are several thousand quantum dots fabricated on the sample; this approach makes it more likely to find at least one dot by doing topography with STM. Still the magnitude of the square is just about enough to have a realistic chance of finding a dot by STM. This is because the coarse positioning of our scanning microscope is about 1 mm, and hence to find a dot by doing topography, the tip would need to land at worst 1 mm (laterally) from the pattern, after it approaches the sample. The reason the gates are fabricated in this particular pattern instead of circular holes within deposited metal is that it would have required immense e-beam writing time to write such a huge pattern, with a lower dose. Using higher dose shortened the time, but destroyed the holes due to proximity effect. Negative e-beam resist (NEB22) was tried in

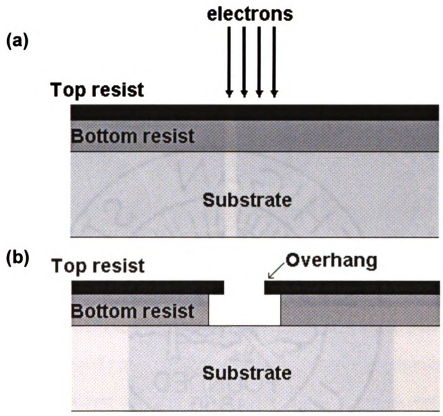

Figure 34. Two layer resist process. (a) The resists are exposed to a beam of electrons. (b) Resists after being exposed and developed, the top resist is underdeveloped and creates an overhang.

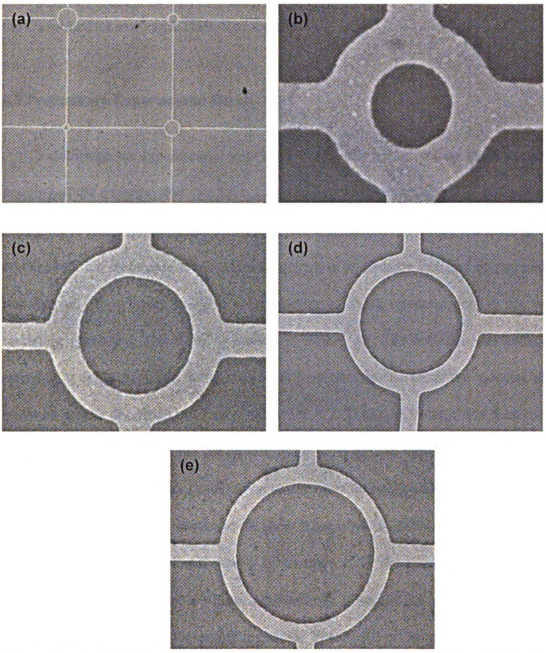

Figure 35. (a) SEM micrograph of the gold gates on GaAs/AlGaAs sample. The circular gates are 12μm apart. (b-e) Further magnified micrographs of individual dots of diameters (b) 0.5μm, (c) 1μm, (d) 1.5μm and (e) 2μm.

order to circumvent this effect, to produce circular holes, but usually failed to adhere to the GaAs surface even with HMDS procedure.

6.3 Preliminary Experimental Result

Although no experimental result has been obtained as yet on the wavefunction imaging of the quantum dots, we have achieved two very important initial goals. First, we were able to find a quantum dot by doing STM. One such STM image is shown in Figure 36. Second, we were able to do addition spectra of a disorder induced quantum dot, to test the validity of using the CAI technique for studying quantum dots in the vertical tunneling geometry. The result is shown in Figure 37. The disorder was induced by applying a large negative voltage (~ -10V) on the tip, to form the circular shaped quantum dot, as described in Chapter 4, Section 4.2. The large voltage was then removed and with the tip fixed over the dot region, its DC voltage was varied from –0.6V to 0.3V. The peaks shown in the plot corresponds to one electron being added to the quantum dot.

This experiment is similar to the pioneering work by Ashoori *et al* [Ashoori 1992, Ashoori 1996], and mentioned briefly in Chapter 1, in the quantum dot section. The difference of course is that we have a tip-induced quantum dot and a tip, instead of a metallic gate, to measure the addition spectra. The width of the peaks is set by the AC excitation, if the rms value of the excitation is greater than kT; otherwise the temperature T sets the width. In our case the excitation amplitude was 5mV rms and indeed the width of the peaks are exactly equal to 5mV. Ideally the peak spacing should be equal. The reason that it is not can be attributed to that fact that the quantum dot potential is not truly parabolic, but has wiggles in it due to disorder. This will lead to unequal spacing of the

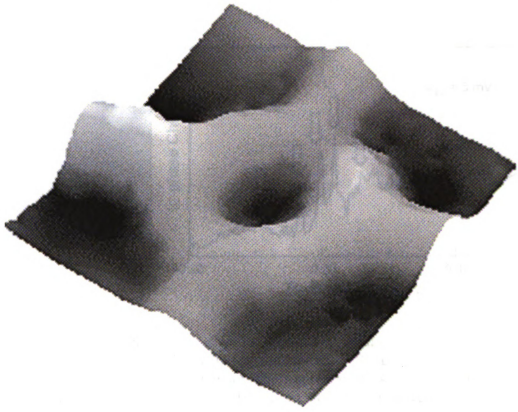

Figure 36. STM image of a quantum dot metallic gate of size 0.5μm.

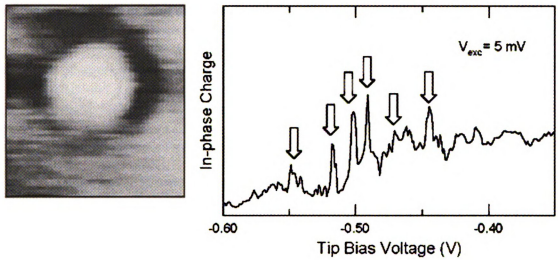

Figure 37. Addition spectra of a disorder induced quantum dot (left). The applied excitation voltage was 5mV. The arrows in the plot show the capacitance peaks, which correspond to one electron entering the dot. There are no peaks seen above the tip voltage of -0.45V, since the energy levels in the dot are too close to be resolved.

energy levels of the quantum dots, which thus leads to unequal peak spacing in our data. Another aspect of the plot is the unequal heights of the peaks. In the ideal case again they should be equal, since either one electron enters the quantum dot or none at all. The heights are not equal because not all the electrons entering the dot, enter below the apex of the tip, and thus exhibit decreased capacitance.

Chapter 7

Summary and future directions

7.1 Summary

In summary, several important goals have been achieved in the course of the research described in this thesis. First, we were able to image the GaAs/AlGaAs 2DES with the CAI technique in the tunneling geometry. This is extremely important since techniques that utilize direct Ohmic contact to the 2DES are not capable of resolving 2DES structure near integer filling [Tessmer 1998, Finkelstein]. The tunneling geometry also provides us information about the tunneling density of states of the 2DES and is sensitive to the psuedogap physics [Eisenstein, Deviatov, Dolgopolov]. With the tunneling geometry, we have observed the charging of the 2DES as a function of the magnetic field. The in-phase charging showed clear dips with 1/B periodicity at integer filling, arising out of quantum Hall physics. The out-of-phase peaks, also observed at integer filling were the signature of the tunneling density of states of the 2DES. We believe they arise from correlation effects that modulate the tunneling density of states, which then result in increased tunneling resistance at integer filling.

We have also imaged the 2DES in this tunneling geometry, and have seen structure near integer filling, which brings us to the second important goal achieved. The observation of orientationally ordered structure in the 2DES near integer filling is the first of its kind to be observed in any geometry. Although the intention of the experiment was to search for periodic structures ("bubbles" and "stripes") with periodicity of 100 nm, stripe like structures were observed near filling factors $\nu = 4$ and 6 with the length scale

an order of magnitude too large. Fourier transforms of the images showed clear orientational order with a length scale of approximately 2 μm. We speculate that the physical origin of the modulations is similar to the CDW theories, but that disorder causes a larger length scale to be selected. Alternatively, the structures may arise from an entirely different mechanism. Clearly, more theoretical work is needed.

The 2DES was also imaged in the absence of a magnetic field to study disorder. Although theories [Efros 1988, Efros 1999, Shklovskii] predict a spatial distribution of the ionized donors to be truly random, observation were made to the contrary. Micron size features were observed, consistent with similar experiments done in the presence of a magnetic field [Tessmer 1998, Finkelstein].

Finally, progress was made to image the wavefunction amplitude of electrons and to study the addition spectra of a quantum dot. The addition spectra of a disorder induced quantum dot was measured, which showed peaks in the in-phase charging at certain values of the tip bias voltage. This measurement was similar to the work of Ashoori *et al* [Ashoori 1992, Ashoori 1996], except a local probe was used for the measurement instead of a fixed metallic gate on the sample.

7.2 Future directions

The CAI technique in the tunneling geometry, which was successfully implemented in the work described in this thesis, holds great promise for future research with 2DES. The future directions of this research can be divided into two broad categories – imaging a 2DES with higher mobility (hence lower density and lower impurities) and imaging electron probability density of single and coupled quantum dots.

With regard to imaging a higher mobility GaAs/AlGaAs sample, it is important to explore the relationship of the stripe-like modulations with disorder. A sample with mobility an order of magnitude higher is already available, provided by Loren Pfeiffer of Lucent Technologies. A study on this sample will provide a critical test for the degree to which disorder alters the stripe-like structure.

The next key issue is to resolve the 2DES structure to smaller length scales, particularly in the length scale predicted to be the periodicity of the CDW patterns. The higher mobility (or lower density) sample has a distinct advantage here. Since the new sample has almost 1/3 the density of the previous sample, the particular Landau level filling factor is reached at about 1/3 the magnetic field. This lower magnetic field value makes the cyclotron radius R_c larger, which finally sets the periodicity of the CDW patterns. In the particular case of filling factor $\nu = 6$ the periodicity is almost 300nm instead of the 95nm calculated in Chapter 5. This value of 300nm is much larger than the spatial resolution of 60nm of our system.

Apart from these two immediate future goals, "spin bottleneck" phenomena can be studied with the 3D-2D tunneling CAI technique. Recent 3D-to-2D tunneling measurements at magnetic fields near $\nu = 1$ have shown that there are two different tunneling rates for charge entering the 2DES [Chan, Deviatov, Dolgopolov]. The fast rate is the usual RC charging time. The slower rate is believed to be the "spin bottleneck" effect, which is a many body phenomenon arising from skyrmion formation in the system [MacDonald]. It essentially reflects a relatively slow electron relaxation time of approximately 1ms. By imaging the 2DES at two different excitation frequencies – one close to the characteristic RC charging time (~ 100kHz) and the other at a much lower

characteristic spin bottleneck frequency (~1kHz) – the spin bottleneck effect and the effect on it due to disorder can be studied [Murthy, Brey, Green, Nazarov].

With regard to quantum dots, the next step is to image the electron wavefunction amplitude and the addition spectra of the individual dots. A future project would be to study coupled quantum dots. When two quantum dots are sufficiently close, tunneling can occur between them. The discrete energy levels of each dot are altered by the presence of the other. This coupled quantum dot system is also called "artificial molecules" [Austing, Brodsky]. It is a very interesting system for studying the competition between kinetic energy and Coulomb interactions in the regimes inaccessible in real molecules. Moreover, such systems may prove to be relevant for quantum computing applications.

REFERENCES

Ashcroft, N. W., and Mermin, N. D., The Drude theory of metals (Chapter 1), in Solid state physics, Saunders College, Philadelphia, 1976.

Ashoori, R. C., Lebens, J. A., Bigelow, N. P., and Silsbee, R. H., Equilibrium Tunneling from the Two-Dimensional Electron Gas in GaAs: Evidence for a Magnetic-Field Induced Energy Gap, Phys. Rev. Lett. 64, 681 (1990).

Ashoori, R. C., Stormer, H. L., Weiner, J. S., Pfeiffer, L. N., Pearton, S. J., Baldwin, K. W., and West, K. W., Single-Electron Capacitance Spectroscopy of Discrete Quantum Levels, Phys. Rev. Lett. 68, 3088 (1992).

Ashoori, R. C., Electrons in Artificial Atoms, Nature 379, 413 (1996).

Austing, D. G., Honda T, Muraki K, Tokura Y, Tarucha S, Quantum dot molecules, physica B 251, 206 (1998).

Ballestad, A., Ruck, B. J., Adamcyk, M., Pinnington, T., and Tiedje, T., Evidence from the Surface Morphology for Nonlinear Growth of Epitaxial GaAs Films, Phys Rev. Lett. 86, 2377 (2001)

Besocke, K., An easily operable Scanning Tunneling Microscope, Surf. Sci. 181, 145 (1987).

Binnig, G., Rohrer, H., Gerber, Ch., and Weibel, E., Tunneling through a controllable vacuum gap, Appl. Phys. Lett. 40, 178 (1982).

Binnig, G., In touch with atoms, Rev. Mod. Phys. 71, S234 (1999).

Brey L, Fertig, H. A., Cote, R., MacDonald, A. H., Skyrme crystal in a 2-dimensional electron gas, Phys. Rev. Lett. 75, 2562 (1995).

Brodsky, M., Zhitenev, N. B., Ashoori, R. C., Pfeiffer, L. N., West, K. W., Localization in artificial disorder: two coupled quantum dots, Phys. Rev. Lett. 85, 2356 (2000).

Chan, H. B., Ashoori, R. C., Pfeiffer, L. N., West, K. W., Tunneling into ferromagnetic quantum Hall states: observation of a spin bottleneck, Phys. Rev. Lett. 83, 3258 (1999).

Chakraborty, Subhasish, Maasilta, I. J., Tessmer, S. H., and Melloch, M. R., Imaging disorder in Two Dimensional Electron System with Charge Accumulation Imaging, Submitted to Phys. Rev. B (Brief Reports).

Cooper KB, Lilly MP, Eisenstein lP, Pfeiffer LN, West KW, Onset of anisotropic transport of two-dimensional electrons in high Landau levels: Possible isotropic-to-nematic liquid-crystal phase transition, Phys. Rev. B 65, 241313, (2002).

Darwin, C. G., The Diamagnetism of the Free Electron, Proc. Cambridge Philos. 27, 86 (1931).

Das Sarma, S., Localization, Metal-Insulator Transitions, and Quantum Hall Effect, in perspectives in Quantum Hall Effects, Edited by S. Das Sarma and A. Pinczuk, John wiley & Sons, New York, 1997.

Davies, J. H., Heterostructures (chapter 3), in The physics of low dimensional semiconductor – An introduction, Cambridge University Press, Cambridge (UK), 1998.

Deviatov, E. V., Shashkin, A. A., Dolgopolov, V. T., Hansen, W., Holland, M., Tunneling measurements of the Coulomb pseudogap in a two-dimensional electron system in a quantizing magnetic field, Phys. Rev. B 61, 2939 (2000).

Dolgopolov, V. T., Drexler, H., Hansen, W., Kotthaus, I. P., Holland, M., Electron correlations and coulomb gap in a 2-dimensional electron-gas in high magnetic-fields, Phys. Rev. Lett. 51, 7958 (1995).

Efros, A. L., Density of states of 2D electron gas and width of the plateau of IQHE, Solid State Commun. 65, 1281 (1988).

Efros AL Electrostatics of an inhomogeneous quantum Hall liquid Phys. Rev. B 60 (19), 13343 (1999).

Eisenstein, J. P., Pfeiffer, L. N., and West, K. W., Coulomb Barrier to Tunneling between Parallel Two-Dimensional Electron Systems, Phys. Rev. Lett. 69, 3804 (1992).

Finkelstein G, Glicofridis PI, Ashoori RC, Shayegan M, Topographic mapping of the quantum hall liquid using a few-electron bubble, Science 289 (5476),90 (2000).

Fock, V., Bemerkung zur Quantelung des Harmonischen Oszillator im Magnetfeld, Z. Phys. 47, 446 (1928).

Fogler, M. M. and Koulakov, A. A., Laughlin Liquid to Charge-Density-Wave Transition at High Landau Levels, Phys. Rev. B 55, 9326 (1997).

Fogler, M. M., Koulakov, A. A., Shklovskii, B. I., Ground state of a two-dimensional electron liquid in aweak magnetic field, Phys. Rev. B 54, 1853 (1996).

Green AG, Kogan II, Tsvelik AM, Skyrmions in the quantum Hall effect at finite Zeeman coupling, Phys. Rev. B 54, 16838 (1996).

Gueret, P., Blanc, N., Germann, R., and Rothuizen, H., Confinement and Single-Electron Tunneling in Schottky-Gated, Laterally Squeezed Double-Barrier Quantum- Well Heterostructures, Phys. Rev. Lett 68, 1896 (1992).

Kastner, M. A., Artificial Atoms, Physics Today 46, 24 (1993).

Koulakov, A. A., Fogler, M. M., Shklovskii, B. I., Charge Density Waves in Two - Dimensional Electron Liquid in Weak Magnetic Field, Phys. Rev. Lett. 76, 499 (1996).

Kouwenhoven, L. P., Oosterkamp, T. H., Danoesastro, M. W. S., Eto, M., Austing, D. G., Honda, T., and Tarucha, S., Exitation Spectra of Circular, Few-Electron Quantum Dots, science 278, 1788 (1997).

Kouwenhoven, L. P., Austing, D. G., and Tarucha, S., Few electron quantum dots, Rep. Prog. Phys. 64, 701 (2001).

Laughlin, R. B., Quantized Hall Conductivity in Two Dimensions, Phys. Rev. B 23, 5632 (1981).

Laughlin, R. B., Anomalous Quantum Hall Effect: An Incompressible Quantum Fluid with Fractionally Charged Excitations, Phys. Rev. Lett. 50, 1395 (1983).

Levi, B. G., Scanning Microscopes Probe Local Details of the Quantum Hall State, Physics Today (Search and Discovery) 51(4), 17 (1998).

Lilly, M. P., Cooper, K. B., Eisenstein, J. P., Pfeiffer, L. N., and West, K. W., Evidence for an Anisotropic State of Two-Dimensional Electrons in High Landau Levels, Phys. Rev. Lett. 82, 394 (1999).

Maasilta, I. J., Chakraborty, Subhasish, Kuljanishvili, I., Tessmer, S. H., and Melloch, M. R., Tunneling images of a 2D electron system in a quantizing magnetic field, Physica E 18 ,167 (2003).

Maasilta, I. J., Chakraborty, Subhasish, Kuljanishvili, I., Tessmer, S. H., and Melloch, M. R., Direct Observation of Micron-Scale Ordered Structure in a Two-Dimensional Electron System, Submitted to Rapid Communications.

Maasilta, I. J., personal communications.

MacDonald, A. H., Spin bottlenecks in the quantum Hall regime, Phys. Rev. Lett. 83, 3262 (1999).

Main, P. C., Beton, P. R., Dellow, M. W., Eaves, L., Foster, T. J., Langerak, C. J. G. M., Renini, M., and Sakai, J. W., Transport in Submicron Resonant-Tunneling Devices, Physica B 189, 125 (1993).

Maksym, P. A., and Chakraborty, T., Quantum Dots in a Magnetic Field: Role of Electron-Electron Interactions, Phys. Rev. Lett. 65, 108 (1990).

McEuen, P. L., Artificial Atoms: New Boxes for Electrons, Science 278, 1729 (1997)

Meirav, U., Kastner, M. A., and Wind, S. J., Single-Electron Charging and Periodic Conductance Resonances in GaAs Nanostructures, Phys. Rev. Lett. 65, 771 (1990).

Mimura, T., HEMT and LSI application (Chapter 4), in Semiconductor and semimetals, Vol. 30, Academic Press Inc., 1990.

Moessner, R. and Chalker, J. T., Exact Results for Interacting Electrons in High Landau Levels, Phys. Rev. B 54, 5006 (1996).

Movsovich, R., in Experimental techniques in condensed matter physics at low temperature (Sec: 3.3), edited by R. C. Richardson and E. N. Smith, Addison-Wesley, New York, 1988.

Murthy G., Effects of disorder on the nu= 1 quantum Hall state, Phys. Rev.B. 64, 241309 (2001).

Nazarov, Y. V., and Khaetskii, A. V., Quantum phase transition in the skyrmion lattice, Phys. Rev. Lett. 80, 576 (1998).

Prange, R. E., Girvin, S. M., The Quantum Hall Effect (2nd Ed.), Springer-Verlag, New York 1987.

Reed, M. A., Randall, J. N., Aggarwal, R. J., Matyi, R. J., Moore, T. M., and Wetsel, A. E., Observation of Discrete Electronic States in a Zero-Dimensional Semiconductor Nanostructure, Phys. Rev. Lett. 60, 535 (1988).

Schmidt, T., Tewordt, M., Blick, R. H., Haug, R. J., Pfannkuche, D., and v. Klitzing, K. Quantum-Dot Ground State in a Magnetic Field Studied by Single-Electron Tunneling Spectroscopy on Double-Barrier Heterostructures, Phys. Rev. B 51, 5570 (1995).

Shklovskii, B. I., and Efros, A. I., Electronic Properties of Doped Semiconductors, Springer- Verlag, New York, 1984.

Smith, T. P., Goldberg, B. B., Stiles, P. J., and Heiblum, M., Direct Measurement of the Density of States of a Two-Dimensional Electron Gas, Phys. Rev. B 32, 2696 (1985).

Stern, F., unpublished internal IBM technical report (1972).

Tarucha, S., Quantum Dots and Artificial Atoms (Chapter 2, Section 2.4), in Mesoscopic Physics and Electronics, Edited by T. Ando, Y. Arakawa, K. Furuya, S. Komiyama, and H. Nakashima. Springer-Verlag, Berlin Heidelberg, 1998.

Tarucha, S., Austing, D. G., Honda, T., van der Hage, R. J., and Kouwenhoven, L. P., Shell Filling and Spin Effects in a Few Electron Quantum Dot, Phys. Rev. Lett. 77, 3613 (1996).

Tessmer, S. R., Glicofridis, P. I., Ashoori, R. C., Levitov, L. S., and Melloch, M. R., Subsurface Charge Accumulation Imaging of a Quantum Hall Liquid, Nature 392, 51 (1998).

Tessmer, S. R., Finkelstein, G., Glicofridis, P. I., Ashoori, R. C., and Melloch, M. R., Modeling subsurface charge accumulation images of a quantum Hall liquid, Phys. Rev. B 66, 125308 (2002).

Tsui, D. C., Stormer, H. L., Gossard, A. C., Two-Dimensional Magnetotransport in the Extreme Quantum Limit, Phys. Rev. Lett. 48, 1559 (1982).

Urazhdin, S., Maasilta, I. J., Chakraborty, S., Moraru, I., Tessmer, S. H., High scan area cryogenic scanning probe microscope, Rev. Sci. Instrum. 71, 4170 (2000).

Urazhdin, S., Tessmer, S. H., Ashoori, R. C., A simple low-dissipation amplifier for cryogenic scanning tunneling microscopy, Rev. Sci. Instrum. 73, 310 (2002).

von Klitzing, K., Dorda, G., and Pepper, M., New Method for High-Accuracy Determination of the Fine-Structure Constant based on Quantized Hall Resistance, Phys. Rev. Lett. 45, 494 (1980).

Wigner, E., On the Interaction of Electrons in Metals, Phys. Rev. 46, 1002 (1934).

Yoo, M. J., Fulton, T. A., Hess, H. F., Willett, R. L., Dunkleberger, L. N., Chichester, R. J., Pfeiffer, L. N., and West, K. W., Scanning Single-Electron Transistor Microscopy: Imaging Individual Charges, Science 276, 579 (1997).

Zhitenev, N. B., Ashoori, R. C., Pfeiffer, L. N., and West, K. W., Periodic and Aperiodic Bunching in the Addition Spectra of Quantum Dots, Phys. Rev. Lett. 79, 2308 (1997).

Zhitenev, N. B., Brodsky, M., Ashoori, R. C., Pfeiffer, L. N., and West, K. W., Localization-Delocalization Transition in Quantum Dots, Science 285, 715 (1999).